ARTICLE IN PRESS

International Journal of Plasticity xxx (xxxx) xxx

FISEVIER

Contents lists available at ScienceDirect

International Journal of Plasticity

journal homepage: www.elsevier.com/locate/ijplas



Predicting textural variability effects in the anisotropic plasticity and stability of hexagonal metals: Application to magnesium and its alloys

Padmeya P. Indurkar a,b, Shahmeer Baweja b, Robert Perez b, Shailendra P. Joshi b,*

- ^a Department of Mechanical Engineering, National University of Singapore, Singapore 117576, Singapore
- ^b Department of Mechanical Engineering, University of Houston, Houston, TX 77204-4006, USA

ARTICLE INFO

Keywords:

Hexagonal close-packed materials Magnesium (Mg) alloys Textural variability Material failure Microstructure-property linkages

ABSTRACT

This work systematically investigates the texture-property linkages in hexagonal close-packed (hexagonal) materials using a three-dimensional computational crystal plasticity approach. Magnesium and its alloys are considered as a model system. We perform full-field, large-strain, micromechanical simulations using a wide range of surrogate textures that sample several experimental datasets for a range of Mg alloys. The role of textural variability and the associated sensitivity of deformation mechanisms on the evolution of macroscopic plastic anisotropy and strength asymmetry is mapped under uniaxial tensile and compressive loading along the material principal and off-axes orientations. To assess the role of crystallographic plastic anisotropy, two distinct material datasets are simulated, which represent pure and alloyed magnesium. The results provide insights into experimental observations reported for magnesium alloys over a range of material textures. We further discuss potential implications on the damage tolerance from the aggregate plastic anisotropy arising from intrinsic crystallographic and textural effects.

1. Introduction

Texture plays an important role in the macroscopic flow stress and deformation stability of hexagonal close-packed (hexagonal) materials. The low crystal symmetry of hexagonal materials often gives rise to remarkable crystallographic plastic anisotropy and tension–compression asymmetry, which propagates through their polycrystalline micromechanics into the macro-scale mechanics. For a given material, the degree to which the single crystal anisotropy and asymmetry of the plastic response is retained at the polycrystalline scale depends on the textural strength, which in turn depends on the processing conditions. As a result, textural control has been an important parameter in the microstructural design of hexagonal materials. Among the class of hexagonal materials, magnesium alloys are exemplars of technological interest in a range of applications (Mordike and Ebert, 2001) — from automotive (Friedrich and Schumann, 2001) to biomedical engineering (Zhang et al., 2009). It is known that texture has an effect on the deformation stability and failure of magnesium alloys (Agnew et al., 2004), which has spawned the interest in designing suitable textures by alloying (Imandoust et al., 2017), or developing novel processing routes (Song et al., 2014), or both.

There exist several experimental investigations on the anisotropic behavior of hexagonal materials. Notable experimental datasets include-monotonic (Agnew and Duygulu, 2005) and cyclic tension-compression as well as simple shear responses of AZ31B Mg sheets (Lou et al., 2007), strain-rate and temperature effects in AZ31 Mg alloys (Khan et al., 2011), large-strain anisotropic tensile and

https://doi.org/10.1016/j.ijplas.2020.102762

Received 23 December 2019; Received in revised form 14 April 2020 Available online 23 April 2020 0749-6419/© 2020 Elsevier Ltd. All rights reserved.

Please cite this article as: Padmeya P. Indurkar, International Journal of Plasticity, https://doi.org/10.1016/j.ijplas.2020.102762

^{*} Corresponding author.

E-mail address: shailendra@uh.edu (S.P. Joshi).

compressive responses in pure titanium (Nixon et al., 2010), among other. Of particular interest here are those that pertain to the role of texture on the large-strain anisotropic response characteristics. Investigations on AZ31 Mg alloys under uniaxial compression (Lee et al., 2011; Foley et al., 2011; Guo et al., 2015) and uniaxial tension (Wang and Choo, 2014) provide insight into the textural effect on the response of Mg alloys (Knezevic et al., 2010). Texture effect on the anisotropic in-plane tensile behaviors of rolled rare-earth Mg alloys (Bohlen et al., 2007) indicate the potential stabilizing effect of textural weakening on the deformation stability, albeit at the cost of depreciated strength. On the other hand, there are relatively sparse experimental datasets reporting both, the tensile and compressive anisotropic behaviors for a fixed initial material state, for example, rolled AZ31 Mg alloy (Kondori et al., 2018) and extruded AM30 Mg alloy (Oppedal et al., 2013). However, these investigations do not explore textural effect.

An allied, much thornier issue is assessing the role of plastic anisotropy in the failure response of hexagonal materials. A working argument, primarily based on formability considerations, is that tempering the plastic anisotropy may be better for ductility. That may not be necessarily optimal under general states and rates of loading, as indicated by recent experiments (Kondori and Benzerga, 2014, 2017; Prasad et al., 2018; Kale et al., 2018) and micromechanical damage theories (Keralavarma et al., 2011). Quantitative connections between the aggregate (crystallographic as well as texture-induced) plastic anisotropy on the modes of failure and ductility are lacking. Experiments indicate that while Mg alloys accumulate internal damage by void evolution, they are notorious to fail by shear banding even under conditions that are highly stiff to shear localization (Kondori and Benzerga, 2014, 2017). In either scenarios, plastic anisotropy plays a key role (Benzerga et al., 2019). Thus, it is important to understand effect of texture on the evolution of macroscopic plastic anisotropy to develop physically relevant models of stability and damage in order to make engineering projections of macroscopic ductility (Lloyd and Priddy, 2017; Basu et al., 2017).

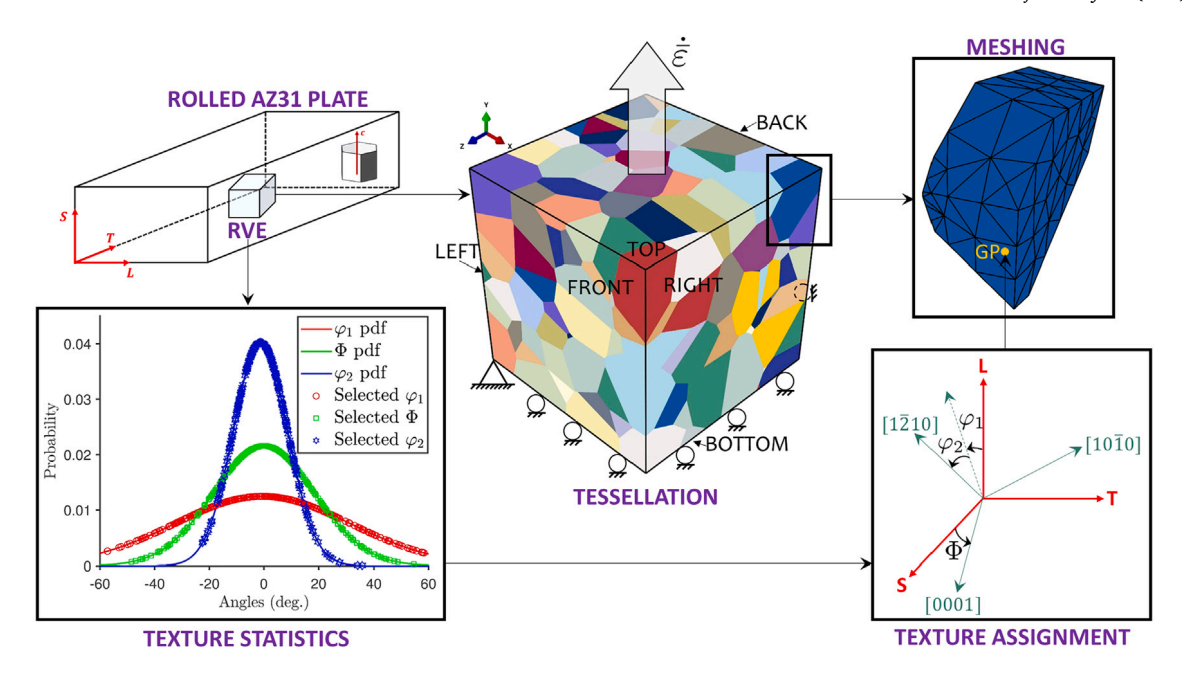
Notwithstanding these developments, a three-dimensional mapping of the textural variability effects on the anisotropic and asymmetric responses is an arduous task. Even in the case of Hill's quadratic anisotropic yield theory (Hill, 1948), one needs uniaxial loading data along the three principal material directions and three off-axis directions to identify all the six anisotropy parameters. Characterizing the yield response of hexagonal materials such as Mg alloys is further complicated by the tension–compression asymmetry (Cazacu and Barlat, 2004). Moreover, barring a few situations (reported in the preceding paragraph), extensive material data-sets may not be available even for a single texture, let alone for a range of textures. Another issue is that available datasets from different test environments typically suffer from variability in the material composition and processing routes, each of which impacts the textural variability.

A potential recourse is to adopt a computational approach that systematically links the anisotropic and asymmetric behaviors of hexagonal materials to textural variability, and makes connections with available experimental observations to enable guidelines for a damage-tolerant material design. Several computational approaches for hexagonal materials exist, including single crystal plasticity (Kalidindi, 1998; Staroselsky and Anand, 2003; Graff et al., 2007), viscoplastic self-consistent modeling (Agnew et al., 2001, 2006; Beyerlein and Tomé, 2008; Nitin et al., 2015), and advanced homogenized continuum theories predicated upon either single surface (Plunkett et al., 2008) or multi-surface (Lee et al., 2008; Steglich et al., 2016) representations of yield surfaces. Some of these approaches enable modeling twinning-detwinning effects (Wang et al., 2012; Qiao et al., 2015), twinning nucleation and propagation (Abdolvand and Daymond, 2013a,b; Cheng and Ghosh, 2015, 2017), and formulating reduced-order models (Wu et al., 2007; Becker and Lloyd, 2016; Kondori et al., 2018). More recent effort in reduced-order representations of polycrystal hexagonal metal plasticity using localization kernels provide avenues to assess a wide spectrum of candidate microstructures in a computationally efficient manner (de Oca Zapiain and Kalidindi, 2019). Initial calibration of the localization kernels must rely on high-fidelity datasets which are typically accessible through crystal plasticity based polycrystal modeling and simulations. Yet, a full three-dimensional computational characterization of the textural interplay with the evolution of plastic anisotropy and tension-compression asymmetry in hexagonal materials has remained largely elusive. With this in mind, we set out to address two objectives in this paper:

- To map the effect of textural variability on the anisotropic and asymmetric macroscopic response of hexagonal materials for different levels of intrinsic crystallographic anisotropy.
 - An associated objective is to synthesize a comprehensive material response dataset (considering textural variations) for calibration, validation and verification of coarse-grained models of hexagonal plasticity.
- To make projections on the effect of aggregate (intrinsic crystallographic and texture-induced) plastic anisotropy on the damage tolerance of hexagonal metals.

We employ a systematic computational program using a three-dimensional finite deformation crystal plasticity framework (Zhang and Joshi, 2012). The constitutive framework has been previously assessed against a range of experiments including nanoindentation (Selvarajou et al., 2014), notched specimens (Selvarajou et al., 2016, 2017; Prasad et al., 2018) and applied to many micromechanical problems of single and polycrystalline Mg (Prasad et al., 2016; Zhang et al., 2016; Selvarajou et al., 2019). The focus here is on modeling the response of magnesium and its alloys. Using the simulation results, we make projections of the role of plastic anisotropy in damage using a micromechanical basis (Basu et al., 2017; Benzerga et al., 2019).

Mathematical preliminaries. Given the second order tensors **A** and **B**, a fourth-order tensor \mathbb{A} , the double contraction **A**: $\mathbf{B} = A_{ij}B_{ij}$, and the contraction \mathbb{A} : $\mathbf{B} = A_{ijkl}B_{kl}$. The inner product $\mathbf{AB} = A_{ik}B_{kj}$, and dyadic product $\mathbf{A} \otimes \mathbf{B} = A_{ij}B_{kl}$. Similarly, given vectors **a** and **b**, we have $\mathbf{a} \otimes \mathbf{b} = a_ib_i$, and $\mathbf{a} \cdot \mathbf{b} = a_ib_i$.



(a) Polycrystalline RVE-FEM model

Fig. 1. Finite element polycrystal RVE setup with kinematic boundary conditions. Textural details are supplied as the variation set of the three Euler angles $[E^{\sigma}] = [\varphi_1^{\sigma}, \Phi^{\sigma}, \varphi_2^{\sigma}]$ to each grain in the RVE. Each grain is discretized using a fine element mesh.

2. Model formulation

2.1. Finite element modeling and texture generation

Three-dimensional Voronoi tessellations of a cubic domain are generated using the Tessellation module (-T) in NEPER (Quey et al., 2011). The cubic domain of dimension L_0 comprises N_g grains. Fig. 1 shows the polycrystal representative volume element (RVE) with $N_g = 300$. The tessellation is kept fixed to mitigate any second-order effects arising from topological deviations. The RVE is meshed using Meshing module (-M) in NEPER with fully integrated tetrahedral finite elements. The discretized RVE is exported to ABAQUS/STANDARD[®], which embeds textural information described in the following paragraph.

Individual grains within the RVE are characterized by distinct crystallographic labels, which are essentially the sets of Euler angles $[E] = [\bar{\varphi}_1 \pm \varphi_1^\sigma, \bar{\Phi} \pm \Phi^\sigma, \bar{\varphi}_2 \pm \varphi_2^\sigma]$, Fig. 1. Each Euler angle is assumed to follow a normal distribution with mean values $[\bar{\varphi}_1, \bar{\Phi}, \bar{\varphi}_2]$ and standard deviations $[\varphi_1^\sigma, \Phi^\sigma, \varphi_2^\sigma]$. Focusing on rolled sheet materials (Kondori and Benzerga, 2014), the texture is assigned as follows: First, each grain g within the RVE is initialized as a single crystal with its principal crystal axes, $[1\bar{2}10], [10\bar{1}0]$ and [0001] respectively aligned with the sheet axes — rolling (L), transverse (T), and the short-transverse (S) directions. Next, setting $\bar{\varphi}_1 = \bar{\Phi} = \bar{\varphi}_2 = 0$, we randomly pick three Euler angles $[E^g] = [\varphi_1^g, \Phi^g, \varphi_2^g]$ from their respective normal distributions (we use the randn function in MATLAB®) that are bounded by $[\pm 3\varphi_1^\sigma, \pm 3\varphi_2^\sigma, \pm 3\varphi_2^\sigma]$ (Fig. 2). Next, a rotation matrix resulting from $[E^g]$ is applied to the initial aligned crystal axes to align it with respect to the sheet axes (L-T-S) (cf. Fig. 1). A second rotation matrix is used to map the L-T-S triad with the global x-y-z triad (loading frame) such that the desired loading direction in the textured material is aligned with the global y-axis, which is kept as the direction of load application for all cases. All the Euler angle sets (E^g) are accounted for with this additional rotation to achieve the textured crystal geometry aligned along loading direction. For more details, the reader is referred to Supplementary Material (Section S-1). Using this procedure, we construct eleven material textures (Fig. 2 plotted using MTEX (Bachmann et al., 2010)), which span a sub-space of the so-called fundamental zone (Bunge, 2013; Wu et al., 2007). These textures sample typical experimental rolled textures, Table 1. Fig. 2l summarizes the maximum intensities of the simulated textures for the eight cases.

A nominal strain-rate ($\dot{\epsilon} = 1 \times 10^{-3} \text{ s}^{-1}$) is applied along the global *y*-direction, Fig. 1. Table 2 consolidates the six uniaxial loading conditions, which include three principal (L, T, S) and three off-axes (LT, LS, TS) material orientations. To ensure a uniaxial stress-state, $\dot{\epsilon}$ is applied at the mid-node of the RVE top-face while the bottom-face is constrained from translating along the *y*-direction, which also eliminates any rigid rotations about the *x*- and *z*-directions. Similarly, the left-face is constrained from translating along *x*-direction, which arrests rigid rotations about *y*-axis. Intersection node of the front, left and bottom faces is pinned to constrain translation along the *z*-axis. The top, right and back faces of the RVE move in response to $\dot{\epsilon}$ such that the volume averaged stresses, $\Sigma_{xx} = \Sigma_{zz} = 0$. Hence, the macroscopic stress-state generated in the RVE is $\Sigma = \Sigma_{yy} (\mathbf{e}_y \otimes \mathbf{e}_y)$, where \mathbf{e}_y is the unit vector in the *y*-direction. The macroscopic logarithmic state of strain generated by this stress state is: $\mathbf{E} = \mathbf{E}_{xx} (\mathbf{e}_x \otimes \mathbf{e}_x) + \mathbf{E}_{yy} (\mathbf{e}_y \otimes \mathbf{e}_y) + \mathbf{E}_{zz} (\mathbf{e}_z \otimes \mathbf{e}_z)$,

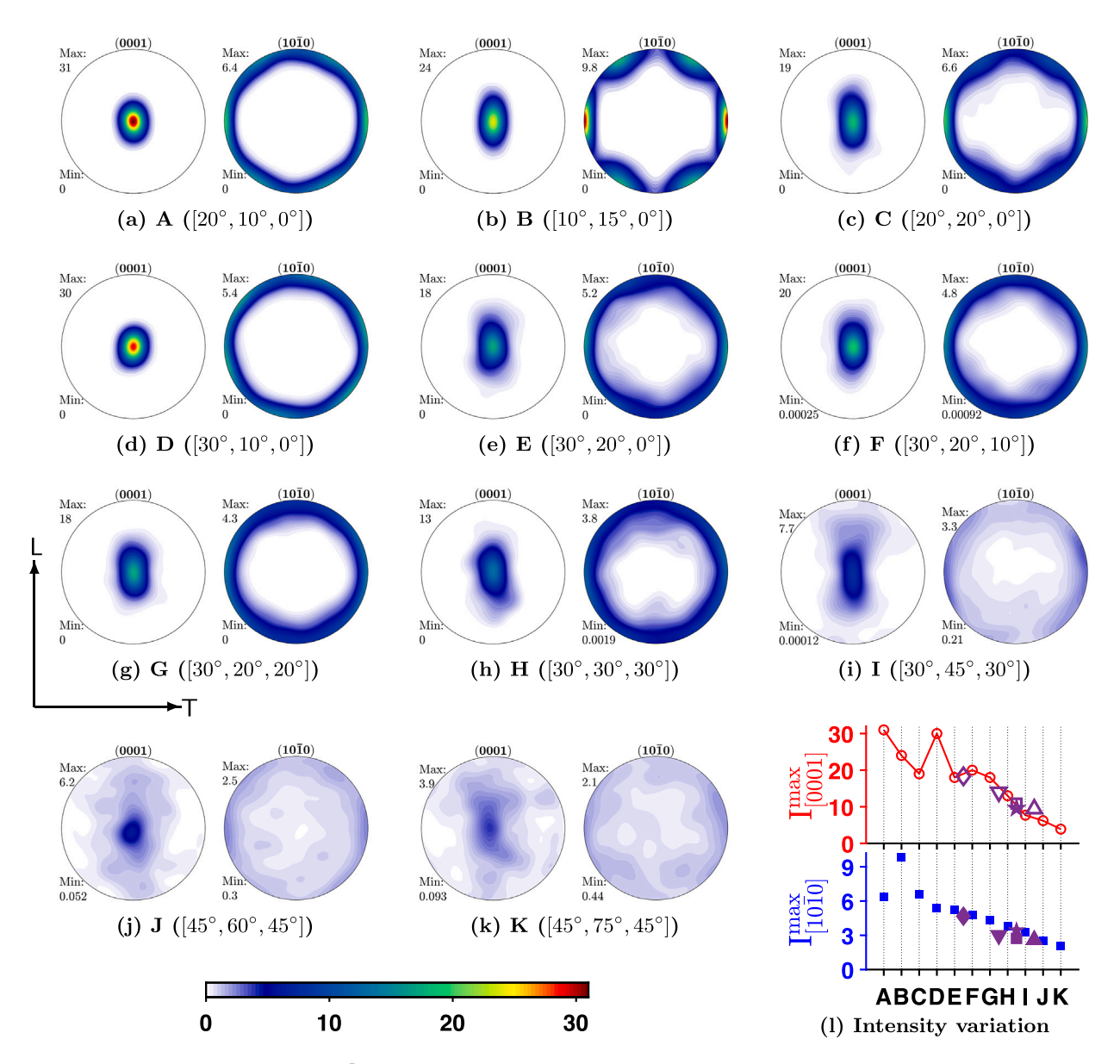


Fig. 2. Panels (a)–(k) show initial [0001] and [1010] pole figures projected on the LT plane for cases A–K, with the respective $E^{\sigma} = [\varphi_1^{\sigma}, \Phi^{\sigma}, \varphi_2^{\sigma}]$ shown in brackets. Panel (l) shows the variation of maximum intensity of [0001] and [1010] crystallographic axes (i.e. $I_{[0001]}^{max}$ and $I_{[1010]}^{max}$ in top and bottom subplots respectively) in these pole figures as function of varying texture cases A–K. In panel (l) the added hollow and solid symbols are texture intensities from references enlisted in Table 1, i.e. Ref. Lou et al. (2007) (\square , \blacksquare), Ref. Hong et al. (2010) (\diamondsuit , \spadesuit), Ref. Khan et al. (2011) (\star , \star), Ref. Wang and Choo (2014) (∇ , \blacktriangledown), Ref. Guo et al. (2015) (\vartriangle , \blacktriangle).

Table 1
Peak [0001] and [10 $\bar{1}$ 0] LT plane pole figure intensities ($I_{[0001]}^{max}$, $I_{[10\bar{1}0]}^{max}$) for different initial synthetic textures. Typical peak intensities reported in literature are included for comparison (cf. Fig. 2).

| I (MRD units) | A (sharp) | E (inter- mediate) | H (weak) | K (weakest) | Lou et al. (2007) | Hong et al. (2010) | Khan et al. (2011) | Wang and Choo (2014) | Guo et al. (2015) | Miller et al. (2016) (AZ61L) |
|----------------------------------|--------------|-----------------------|-------------|----------------|----------------------|--------------------|--------------------|-------------------------|----------------------|------------------------------------|
| Imax [0001] Imax [1010] | 31.0 6.4 | 18.0 5.2 | 13.0 3.8 | 3.9 2.1 | 10.9 3.0 | 18.3 4.7 | 9.6 3.0 | 14.0 3.14 | 9.43 2.6 | 11.8, 7.7, 5.6 3.2, 2.3, 1.8 |

Table 2 Loading cases for each texture and material dataset. The relation between the global loading directions (x-y-z) and the material directions (L-T-S) is shown. () $^{\perp}$ indicates a direction perpendicular to the direction ().

| Loading direction (along y) | L | T | S | LT | LS | TS |
|-----------------------------|---|---|---|--------------|--------------|--------------|
| Lateral direction (along x) | T | L | L | LT^{\perp} | LS^{\perp} | L |
| Lateral direction (along z) | S | S | T | S | T | TS^{\perp} |

Table 3
Slip and twin systems observed in Mg single crystals.

| Mechanisms | Slip/twin plane | Slip/twin direction | No. of systems |
|--|-----------------|-----------------------------------|----------------|
| Basal ⟨a⟩ slip | (0001) | ⟨1120⟩ | 3 |
| Prismatic $\langle a \rangle$ slip | {1010} | ⟨1120⟩ | 3 |
| Pyramidal $\langle a \rangle$ slip | {1011} | ⟨1120⟩ | 6 |
| Pyramidal $\langle c + a \rangle$ slip | {1122} | ⟨1123⟩ | 6 |
| Extension twinning | {1012} | ⟨10Ī1⟩ | 6 |
| Contraction twinning | {1011} | $\langle 10\bar{1}\bar{2}\rangle$ | 6 |

where $E_{xx} = \ln(L_x/L_0)$, $E_{yy} = \ln(L_y/L_0)$ and $E_{zz} = \ln(L_z/L_0)$. The Lankford (lateral strain) ratio is calculated as E_{xx}/E_{zz} , where the x- and z-directions depend on the loading direction under consideration (Table 2). The von Mises equivalent stress is: $E_{eq} = \sqrt{(3/2)\Sigma' : \Sigma'} = |\Sigma_{yy}|$ and the corresponding effective strain is: $E_{eq} = \sqrt{(2/3)E' : E'}$ where Σ' are the deviatoric stresses and E' are the corresponding deviatoric strains.

2.2. HCP Mg crystal plasticity FE model

The constitutive material considered here comprises of eighteen slip systems and twelve twin systems (Table 3) and a finite strain rate-dependent viscoplastic flow rule is employed for each of these plasticity modes with rate-tangent method, followed with twinning/spin induced lattice reorientation described next in this section.

The transversely isotropic elastic response is characterized by five independent constants ($C_{11} = 59.40$ GPa, $C_{12} = 25.61$ GPa, $C_{13} = 21.40$ GPa, $C_{33} = 61.60$ GPa and $C_{44} = 16.40$ GPa). The total deformation gradient **F** is multiplicatively decomposed into elastic **F**^e and plastic **F**^p components, i.e. **F** = **F**^e**F**^p. The spatial velocity gradient is the sum of an elastic (\mathbf{L}^e) and a plastic (\mathbf{L}^p) part.

$$\mathbf{L} = \dot{\mathbf{F}}\mathbf{F}^{-1} = \mathbf{L}^e + \underbrace{\mathbf{F}^e \tilde{\mathbf{L}}^p \left(\mathbf{F}^e\right)^{-1}}_{\mathbf{L}^p}$$
(1)

where $\dot{\mathbf{F}}$ is the material derivative of \mathbf{F} . The plastic velocity gradient (\mathbf{L}^p) is computed in the current configuration as the sum of two parts: slip in the parent region and twin in the parent region,

$$\mathbf{L}^{p} = \underbrace{\left(1 - \sum_{\beta=1}^{N_{tw}} f^{\beta}\right) \sum_{\alpha=1}^{N_{s}} \dot{\gamma}^{\alpha} (\mathbf{s}^{\alpha} \otimes \mathbf{m}^{\alpha})}_{slip \ in \ parent} + \underbrace{\sum_{\beta=1}^{N_{tw}} \dot{\gamma}^{\beta} (\mathbf{s}^{\beta} \otimes \mathbf{m}^{\beta})}_{twin \ in \ parent}$$

$$(2)$$

where α and β refer to slip systems and twin systems in the parent region respectively; the model accounts for $N_s=18$ slip and $N_{tw}=12$ twin systems respectively (cf. Table 3). The shear rate on the *i*th system is denoted by $\dot{\gamma}^i$ where $i=\alpha$ or β . The twin volume fraction of the β th twin system is denoted as f^{β} . The slip/twin plane normal and direction vector of the *i*th system, in the current configuration, are denoted as \mathbf{m}^i and \mathbf{s}^i respectively. The constitutive relations for slip and twinning are briefly described (see Zhang and Joshi, 2012 for details):

1. Constitutive equations for slip: The slip rate $\dot{\gamma}^i$ on the *i*th slip system is described by a visco-plastic power law:

$$\dot{\gamma}^i = \dot{\gamma}_0 \left| \frac{\tau^i}{\sigma^i} \right|^{1/m} \operatorname{sgn}(\tau^i) \quad (i = \alpha \text{ or } \tilde{\alpha})$$
(3)

where $\tau^i = \sigma$: $(\mathbf{m}^i \otimes \mathbf{s}^i)$ is the resolved shear stress (RSS) based on the Schmid law and g^i is the current strength of the *i*th slip system. The reference slip rate $\dot{\gamma}_0 = 0.001 \text{ s}^{-1}$ and the rate-sensitivity exponent m = 0.02. g^i is calculated as the sum of the initial strength (τ^i_0) , incremented by the hardening due to slip-slip (\dot{g}^i_{sl-sl}) and twin-slip (\dot{g}^i_{lm-sl}) interactions:

$$g^{i} = \tau_{0}^{i} + \int_{t_{0}}^{t_{i}} (\dot{g}_{sl-sl}^{i} + \dot{g}_{tw-sl}^{i}) \, dt \tag{4}$$

 \dot{g}_{sl-sl}^{i} is given by

$$\dot{g}_{sl-sl}^i = \sum_{i=1}^{N_s} h_{ij}(\bar{\gamma})\dot{\gamma}^j \tag{5}$$

where h_{ij} is the hardening modulus for self (i = j) and latent $(i \neq j)$ hardening. h_{ij} depends on the total accumulated shear strain $(\bar{\gamma})$ on all slip systems, i.e. $\bar{\gamma} = \sum_{i=1}^{N_s} \int_{t_0}^{t_i} \dot{\gamma}^i$. Further, h_{ij} is defined as:

$$h_{ij} = \begin{cases} h(\bar{\gamma}) & (i=j) \\ qh(\bar{\gamma}) & (i\neq j) \end{cases}$$
 (6)

for latent hardening $1 \le q \le 2$; here we take q = 1. A linear non-saturation type hardening law is used for basal slip whereas a saturation type hyperbolic hardening function is employed for the non-basal slip modes,

$$h(\bar{\gamma}) = \begin{cases} h_0, & \text{(basal slip)} \\ h_0^i \text{sech}^2 \left| \frac{h_0^i \bar{\gamma}}{r_s^i - r_0^i} \right|, & \text{(non-basal slip)} \end{cases}$$
 (7)

where h_0^i is the initial hardening modulus and τ_s^i is the saturation stress of the *i*th slip system.

2. **Constitutive equations for twinning:** The rates of extension (ET) and contraction twinning (CT) volume fraction (v.f.) in the parent region are described as:

$$\dot{f}^{\beta} = \begin{cases} \dot{f}_{et}^{0} \left(\tau^{\beta} / s_{et}^{\beta} \right)^{1/m_{t}}, & \text{(ET)} \\ \dot{f}_{ct}^{0} \left(\tau^{\beta} / s_{ct}^{\beta} \right)^{1/m_{t}}, & \text{(CT)} \end{cases}$$

where τ^{β} is the RSS and s^{β} is the current strength of the β^{th} twin system. The average reference twin v.f. evolution rates of ET and CT are $\dot{f}_{et}^0 = 0.001 s^{-1}$ and $\dot{f}_{ct}^0 = 0.001 s^{-1}$. The rate-sensitivity exponent $m_t = 0.02$ for both, ET and CT systems. The rate of plastic shear $\dot{\gamma}^{\beta}$ on β^{th} twin system is related to \dot{f}^{β} via:

$$\dot{\gamma}^{\beta} = \dot{f}^{\beta} \gamma^{tw} \tag{9}$$

where γ^{tw} is the theoretical twinning shear. For Mg, $\gamma^{tw}=0.129$ and 0.138 for ET and CT respectively. s^{β} is calculated as the sum of the initial CRSS $\left(\tau_{0}^{\beta}\right)$, incremented by the hardening due to twin-twin \dot{s}_{tw-tw}^{β} and slip-twin \dot{s}_{sl-tw}^{β} interactions,

$$s^{\beta} = \tau_0^{\beta} + \int_{t_0}^{t_i} (\dot{s}_{tw-tw}^{\beta} + \dot{s}_{sl-tw}^{\beta}) \, \mathrm{d}t \tag{10}$$

The hardening of ET systems due to twin-twin interaction follows a hyperbolic function,

$$\dot{s}_{tw-tw}^{\beta} = h_{\text{et}}^{\beta} \operatorname{sech}^{2} \left| \frac{h_{\text{et}}^{\beta} \bar{\gamma}_{et}}{\tau_{e,et}^{\beta} - \tau_{0,et}^{\beta}} \right| \dot{\gamma}^{\beta} \tag{11}$$

where h_{et}^{β} is the initial hardening modulus and $\tau_{s_et}^{\beta}$ is the saturation stress for ET. $\bar{\gamma}_{et}$ is the total shear strain on all ET systems. On the other hand, CT hardening is assumed to be of non-saturation type,

$$\dot{s}_{tw-tw}^{\beta} = H_{ct} \left(\sum_{m=1}^{N_{ct}} f^m \right)^b \dot{\gamma}^{\beta} \tag{12}$$

where N_{ct} is the total number of CT systems. H_{ct} and b are hardening parameters for CT.

The hardening of the twin systems evolve independent of the slip in the crystal (Zhang and Joshi, 2012), i.e. hardening of the twin systems due to slip activity \dot{s}^i_{sl-tw} is taken to be zero. On the other hand, twinning is assumed to affect the slip hardening, and the term \dot{g}^i_{tw-sl} in Eq. (4) is given by

$$\dot{g}_{tw-sl}^{\beta} = \begin{cases} h_{et_sl}^{\beta} \operatorname{sech}^{2} \left| \frac{h_{et_sl}^{\beta} \bar{\gamma}_{et}}{\tau_{s_et}^{\beta} - \tau_{0_et}^{\beta}} \right| \dot{\gamma}^{\beta}, & (ET) \\ 0.5 H_{ct_sl} (\bar{\gamma}_{ct})^{-0.5} \dot{\gamma}_{ct}, & (CT) \end{cases}$$
(13)

For a particular twin mode, when the total twin volume fraction on all its twin systems reaches a critical value f_{cr} (set equal to 0.9) the FE volume represented by that GP is reoriented from its original orientation to the twinned one; the twin system that possesses the largest twin v.f. is chosen as the orientation of the twinned lattice. A detailed algorithmic description of this scheme and its FE implementation can be found in (Zhang and Joshi, 2012). Table 4 consolidates the single crystal material parameters in Eq. (3) through (13) for both, pure and alloyed Mg (the sources are reported in the table). The volume averaged relative activity $\bar{\xi}^i$ for *i*th deformation mode is given as:

$$\bar{\xi}^{i} = \frac{\int \Delta \gamma^{i} \, \mathrm{d}V}{\int \sum_{i=1}^{N_{s}+N_{tw}} \Delta \gamma^{i} \, \mathrm{d}V}$$
(14)

where Δy^i is the incremental shear strain from *i*th mode at each integration point. The integration is performed over the domain volume.

Table 4
Material parameters^a for Mg alloy AZ31 and (in brackets) pure Mg.

| Mechanism | τ_0 (MPa) | h_0 (MPa) | τ_s (MPa) | | $\tau_0^i/\tau_0^{\mathrm{pris.}\langle a\rangle\mathrm{sl.}}$ |
|--|----------------------|-----------------------|--------------------------|--------------------|--|
| Basal ⟨a⟩ slip | 10 (0.5) | 50 (20) | - | | 0.18 (0.02) |
| Prismatic $\langle a \rangle$ slip | 55 (25) | 1500 | 110 (85) | | 1 |
| Pyramidal $\langle a \rangle$ slip | 55 (25) | 1500 | 110 (85) | | 1 |
| Pyramidal $\langle c + a \rangle$ slip | 60 (40) | 3000 | 170 (150) | | 1.09 (1.6) |
| | τ ₀ (MPa) | h _{et} (MPa) | τ _{s et} (MPa) | h_{et_sl} (MPa) | |
| Extension twinning | 15 (3.5) | 120 (100) | 30 (20) | 100 | 0.27 (0.14) |
| | τ ₀ (MPa) | H _{ct} (MPa) | H _{ct sl} (MPa) | b | |
| Contraction twinning | 85 (55) | 6000 | 15 | 0.05 | 1.55 (2.2) |

aCRSS and hardening parameters adopted from Lou et al. (2007), Hutchinson and Barnett (2010), Agnew et al. (2003), Hong et al. (2010) and Selvarajou et al. (2016, 2017) for Mg alloy and from Zhang and Joshi (2012) for pure Mg.

3. Simulation results

The simulations are performed using mesh discretization of nearly 84,000 fully integrated linear tetrahedral finite elements with approximately 279 elements per grain. The reader is referred to Supplementary Material (Section S-2) for the mesh convergence study.

3.1. Tensile loading along the principal axes

Figs. 3 and 4 respectively show the polycrystalline tensile and compressive responses for the eleven texture cases (Table 2) when loaded uniaxially along the three principal directions: L, T and S. In the figures, the black solid lines with symbols indicate the mean of the eight responses while the shaded regions indicate one standard deviation about the mean for the $\Sigma_{eq} - E_{eq}$ and R plots. For the relative activity plots, the shaded regions denote 0.674 times standard deviation for relative activity plots (i.e. encompassing 50% of the data).

Focusing first on the in-plane directions (L, T), the textural variability for cases A–H has a small effect on the variability of the tensile stress–strain responses in the sheet rolling (L, Fig. 3a) and transverse (T, Fig. 3d) directions, and it tends to further decrease with increasing strain. Between them, the textural variability has a smaller effect on the T-direction stress–strain response deviation compared to the L-direction. In comparison, cases I through K exhibit a significant deviation from their predecessors. Clearly, these three weakest textures fall outside of the standard deviation. Of particular significance is the difference in the stress–strain response of case I relative to case H, where the deviation in Φ^{σ} appears to have a strong influence in weakening the response for case I. Interestingly though, the same effect is not observed amongst cases J and K for which the difference in Φ^{σ} is similar, for fixed φ_1^{σ} and φ_2^{σ} .

On the other hand, remarkable variability is seen in the lateral strain responses for both, L and T directions (cf. Figs. 3b and 3e), particularly between cases A–H. In fact, the variability increases with increasing applied strain. In comparison, cases I–K exhibit much tempered strain anisotropy for both L and T tension, which is reminiscent of some Mg rare-earth alloys (e.g. WE43: Kondori and Benzerga, 2015, AMX602: Meredith et al., 2016, ZEK100: Habib et al., 2017, 2019).

Among the three Euler angles, variability of Φ^{σ} plays a stronger role in the response variations with φ_{1}^{σ} playing a secondary role. For a fixed φ_{1}^{σ} , increasing Φ^{σ} leads to a decrease in both the tensile stress and the lateral anisotropy ratios R_{L}^{T} and R_{T}^{T} . This effect increases with increasing φ_{1}^{σ} . As such, case K gives the weakest stress–strain response but also produces a near-isotropic lateral deformation. Note that the variability of the strain anisotropy is higher for the T-direction compared to the L-direction. The variability of φ_{2}^{σ} seems to have a non-monotonic effect. Over a certain range, the stresses tend to be higher and strains more anisotropic with increasing φ_{2}^{σ} ; for example, comparing cases and $E(\varphi_{2}^{\sigma}=0^{\circ})$, F $(\varphi_{2}^{\sigma}=10^{\circ})$, and G $(\varphi_{2}^{\sigma}=20^{\circ})$ we see that case G > case F > case E. However, a further weakening of φ_{2}^{σ} (case H $[E^{\sigma}]=[30^{\circ},30^{\circ},30^{\circ}]$) produce the softest stress–strain responses and the lowest lateral anisotropy in both, L and T loading directions. Consider the two pairs of textures — [J,K] and [H,I]. The diminished sensitivity of the incremental stress weakening $(\Delta \Sigma = \Delta \Sigma_{[J,K]} - \Delta \Sigma_{[H,I]})$ and lateral strain ratio $(\Delta R = \Delta R_{[J,K]} - \Delta R_{[H,I]})$ between these paired cases hint at the competition between Φ^{σ} and φ_{2}^{σ} . While a higher Φ^{σ} tends to weaken the stress and assist isotropic deformation, a higher φ_{3}^{σ} has the opposite effect.

The averaged relative activities (Eq. (14)) of individual deformation mechanisms (cf. Figs. 3c, 3f) link the textural variability to the variability in the macroscopic responses. The non-basal modes prismatic $\langle a \rangle$ slip and pyramidal $\langle a \rangle$ slip are the primary deformation mechanisms uniaxial tension along the L and T directions (as expected), but the relatively harder non-basal pyramidal $\langle c + a \rangle$ slip mode is also important. Interestingly, the variation of prismatic $\langle a \rangle$ slip is much higher than the other deformation modes. Seen differently, the large variability in the prismatic $\langle a \rangle$ slip is nearly equally compensated by the variability of the other active deformation modes. At early stages of deformation, basal $\langle a \rangle$ slip shows a high activity (initial $\bar{\zeta}^{\text{basal}} > 0.60$ for the weak texture cases H-K), although it decreases with strain.

The trends of the relative activities and their variability explain the dichotomy in the disparate sensitivities of the flow stress and strain anisotropy to initial texture. The non-basal modes possess similar strength parameters, which explains the relatively low sensitivity of the stress–strain responses to textural variations. On the other hand, the macroscopic strain accumulated in the two

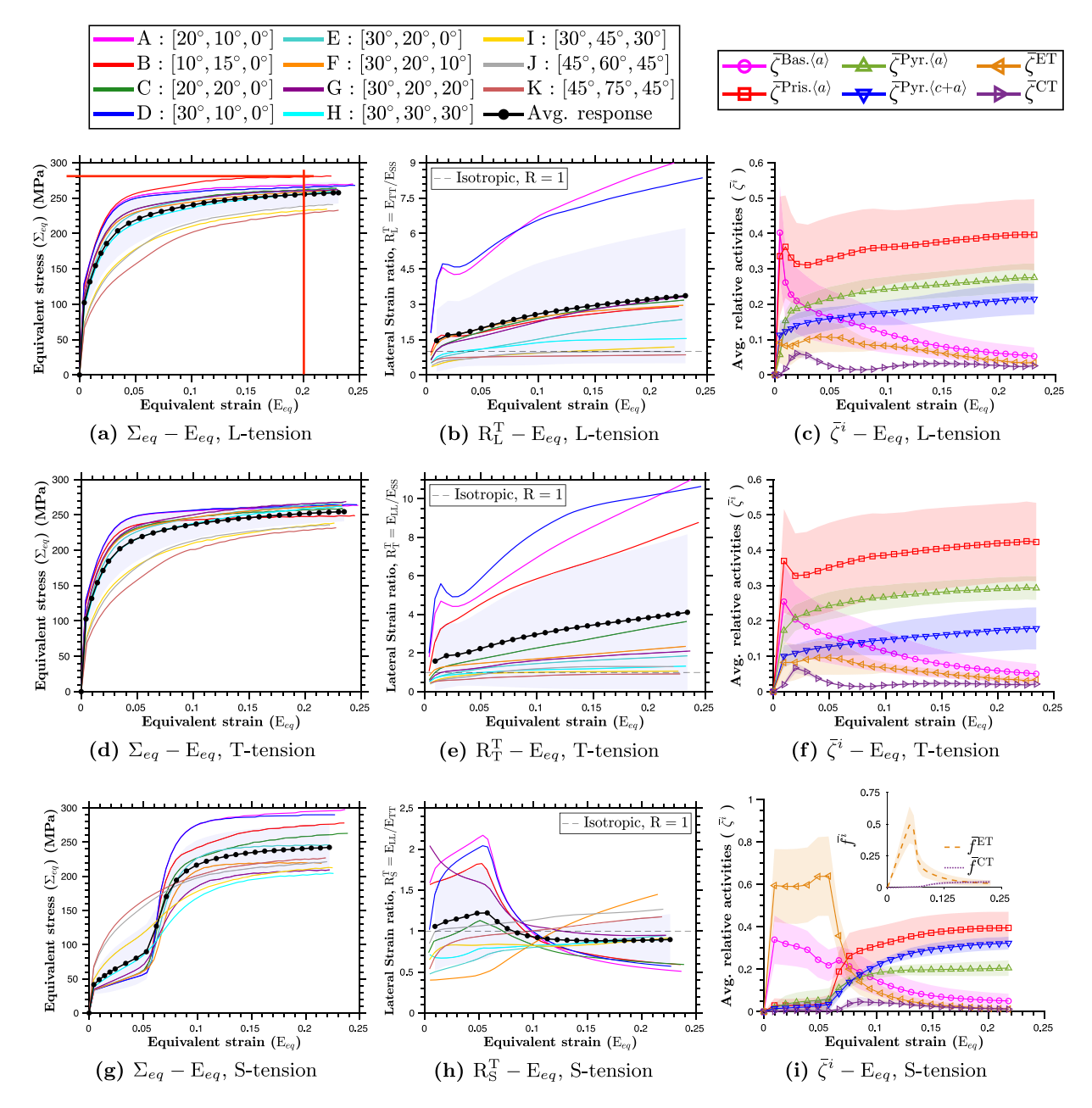


Fig. 3. Uniaxial tension along principal material directions L,T and S. Texture effects on the evolution of (i) equivalent stress-equivalent strain (panels (a, d, g)), (ii) lateral strain ratio (panels (b, e, h)), and (iii) relative activities of deformation mechanisms (panels (c, f, i)).

lateral directions has contributions from the shear strains projected from the slip systems to those directions, which vary substantially with textural variations. For instance, consider a sharp textured material (in the limit of a single crystal) loaded in tension along the T-direction (aligned with the y-axis). For the same incremental shear strain ($\Delta \gamma$) accrued on the prismatic $\langle a \rangle$ slip variant $(01\bar{1}0)[2\bar{1}\bar{1}0]$ and pyramidal $\langle c+a \rangle$ slip variant $(2\bar{1}\bar{1}2)[\bar{2}113]$, the former will contribute only $0.5\Delta \gamma$ along the x-direction and has no contribution to the z-direction, while the latter projects $0.26\Delta \gamma$ along the x-direction and $0.85\Delta \gamma$ along the z-direction. Notably, both variants demand similar stress increments to cause these deformations. Thus, an increase in the pyramidal $\langle c+a \rangle$ slip activity (at the expense of the prismatic $\langle a \rangle$ slip) effected by textural weakening will not have a major influence on the macroscopic stress, but will certainly increase the lateral strain anisotropy. We note that the lower pyramidal $\langle c+a \rangle$ slip activity in T-tension compared to L-tension ($\sim 67\%$ reduction over cases A–H) results in the plastic anisotropy in an otherwise isotropic LT plane. For a sharp texture, it is a result of the propagation of the Schmid effect in a single crystal where T-tension resolves no shear stress on the two conjugate

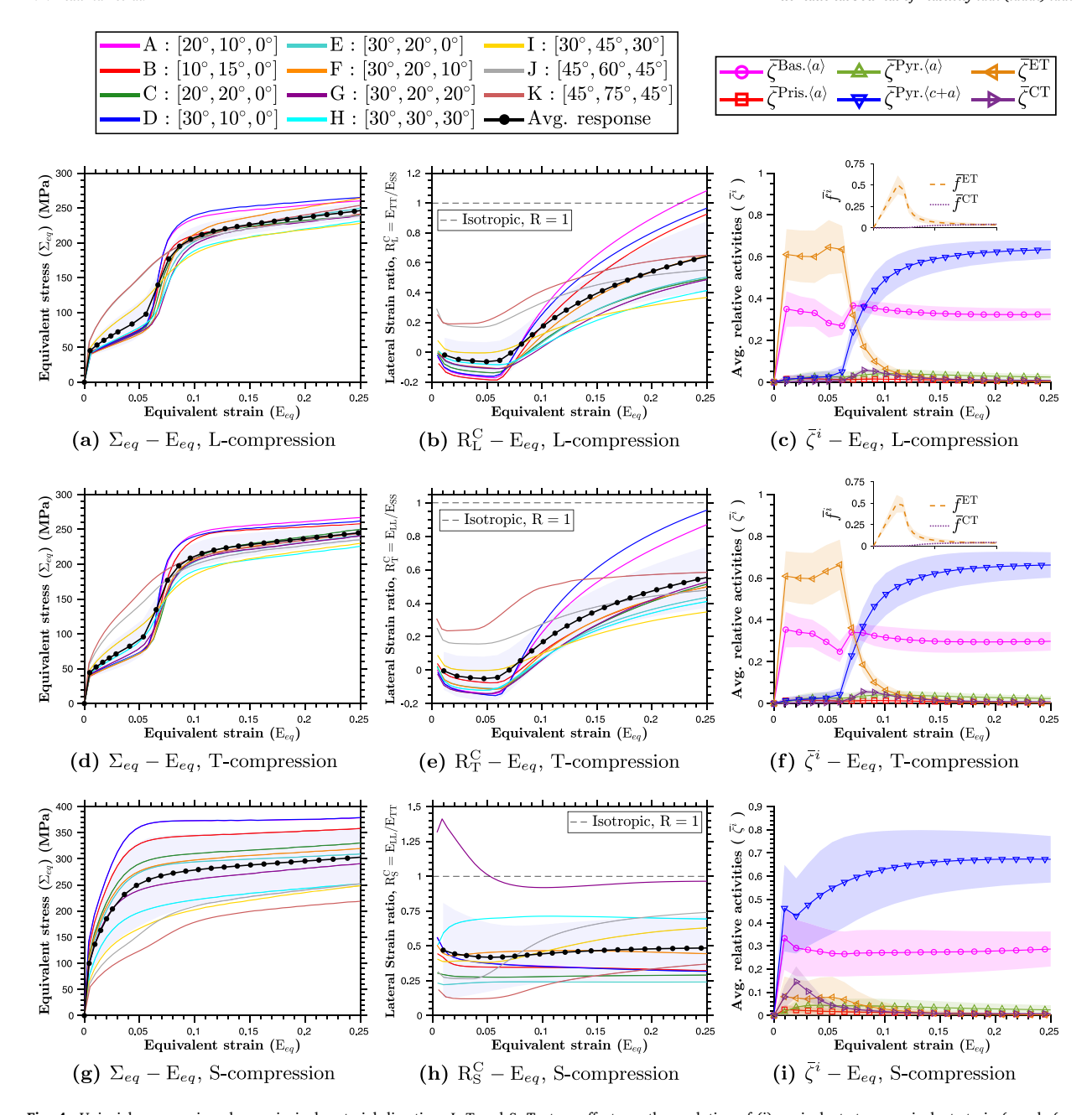


Fig. 4. Uniaxial compression along principal material directions L, T and S. Texture effects on the evolution of (i) equivalent stress-equivalent strain (panels (a, d, g)), (ii) lateral strain ratio (panels (b, e, h)), and (iii) relative activities of deformation mechanisms (panels (c, f, i)).

pyramidal $\langle c + a \rangle$ slip variants, $(\bar{1}2\bar{1}2)[1\bar{2}13]$ and $(1\bar{2}12)[\bar{1}2\bar{1}3]$ while in L-tension all six pyramidal $\langle c + a \rangle$ slip variants experience a non-zero resolved shear stress.

In contrast to the in-plane responses, the S-direction stress–strain responses are generally governed by extension twinning. However, its potency is affected by texture and this coupling is complicated. For cases A-G, the textural variability plays a negligible role in the initial stages of deformation ($E_{eq} \lesssim 0.06$) where extension twinning prevails (cf. Fig. 3g). Only after the twinning effect is complete does the textural variability emerge in the subsequent hardening and flow saturation responses. Case H marks a transition in this trend. Weakening of initial texture from case H to case K brings about a transition from a classical sigmoidal response to a power-law type response. The corresponding relative activity evolution shows increasing importance of $\langle a \rangle$ slip modes in lieu of extension twinning as a result of weaker basal pole intensities (cf. Figs. 2j, 2k). The flow stress at large strains exhibits a strong sensitivity to textural variations that is non-monotonic. Interestingly, the weakest saturated flow stress occurs for case H, which

International Journal of Plasticity xxx (xxxx) xxx

P.P. Indurkar et al.

is not the weakest texture. The strongest (i.e. case A) and the weakest responses (i.e. case H) deviate nearly 20% of the average stress-strain response.

The textural sensitivity of the flow stress saturation in the post-twinned regime may be categorized into five groups: (i) Group-1: [A, D, B]; (ii) Group-2 [C, E]; (iii) Group-3 [F, G]; (iv) Group 4: [H, I], and (v) Group 5: [J, K]. Members of Group-1, which exhibit the strongest twin-induced hardening are characterized by relatively small Φ^{σ} . At the other end, Group-4, which exhibits the weakest twin-induced hardening and Group-5, which exhibits power-law type behavior are characterized by a high Φ^{σ} . Group-2 and Group-3 are characterized by intermediate values of Φ^{σ} . It is from these cases that we deduce the relative importance of φ^{σ}_1 and φ^{σ}_2 . In Group-2, for a fixed Φ^{σ} , case C (smaller φ^{σ}_1) is stronger than case E (larger φ^{σ}_1), particularly at larger strains. In Group-3 (fixed $[\varphi^{\sigma}_1, \Phi^{\sigma}]$), a smaller φ^{σ}_2 results in a stronger response, cf. case F versus case G. From these observations, φ^{σ}_1 and φ^{σ}_2 have a qualitatively similar effect on the twin-induced hardening as Φ^{σ} , although Φ^{σ} has a dominating influence.

Contrary to the stress–strain responses, the lateral strain anisotropy in S-tension exhibits a high sensitivity to textural variability in both, the twinning-dominated and the post-twinned regimes. Unlike the large ranges of R_L^T and R_T^T , R_S^T spans a relatively narrow range (0.5 $\lesssim R_S^T \lesssim$ 2). For Group-1, in the twinning regime $R_S^T > 1$, which increases with increasing strain until $E_{eq} \leq 0.07$ but decreases rapidly and tends to asymptote to $R_S^T \sim 0.6$, that resemble experimental values (Kondori et al., 2018). For Group-2, $R_S^T \lesssim 1$ over the entire strain range, which signifies that the ability of textures in this family to modulate deformation mechanisms so that the lateral deformation responses are near to isotropic while maintaining a reasonable strengthening behavior.

Finally, the R_S^T ratios are further tempered in members of Group-3 and Group-4 but also exhibit weaker hardening responses. In comparison, Group-5 shows a better combination of higher saturation and lower deformation anisotropy with increasing Φ^{σ} . We note in passing that the distinction between the tensile behaviors along L, T, and S directions practically disappear for cases J and K.

The foregoing observations have clear underpinnings in the corresponding deformation mechanisms as laid out in Fig. 3i. The relative insensitivity of the flow stress to textural variability in the twinning regime (cases A-G) arises from the similarities in the strengthening potencies of extension twinning and basal $\langle a \rangle$ slip (the latter is promoted in weaker textures). Yet, the relative contributions of these mechanisms to the macroscopic lateral strains is distinct, and therefore, R_S^T variability delicately depends on the textural variability through the projections via Schmid factors at the grain scale. In a strongly textured material, the twin systems tend to contribute nearly equally to the lateral plastic strains ($R_S^T \sim 1$), but for a weakly textured material, one of the lateral directions attracts more contribution from twinning than the other, resulting in either $R_S^T > 1$ or $R_S^T < 1$.

3.2. Compressive loading along the principal axes

Fig. 4 consolidates the compressive responses along L, T, and S directions. The twinning dominated responses along the L and T directions exhibit characteristics that are broadly similar to those reported for the tensile response along the S direction (cf. Fig. 3g). The variability in the stress–strain behaviors under L-compression and T-compression is relatively smaller compared to S-tension. Notably, case H does not exhibit the kind of departure seen in S-tension. Moreover, while the S-tension responses exhibit near-perfect plasticity beyond the rapid twin-induced hardening, compression along L and T induces a mild but finite material hardening in the same regime. Overall, the hardening is weakened with increasing textural variability with primary effect from Φ^{σ} and progressively smaller influences from φ_2^{σ} and φ_1^{σ} . As in the case of S-tension, the L-, T-compression responses for cases J, K show power-law type behaviors

Despite broader similarities with the S-tension stress-strain responses, the lateral strain anisotropy behaviors under L and T compression ($R_{\underline{C}}^{L}$ and $R_{\underline{C}}^{T}$, Fig. 4b) are remarkably different compared to $R_{\underline{S}}^{T}$. First, both ratios transition from a negative value to a positive value with deformation (excluding cases I-K) — a phenomenon not observed in S-tension (cf. Fig. 3h). This transition coincides with the equivalent strain at which twin-induced rapid hardening sets in. Cases J and K do not exhibit this behavior. Case I is peculiar in that the initial deformation response indicates practically no straining along one lateral direction $(R_T^C \approx R_T^C \approx 0)$ in the twinning regime before gradually increasing to positive values. Second, although $R_L^C o 1$ with increasing deformation it occurs at a much slower rate compared to S-tension. Furthermore, the deformation anisotropy is more significant in this loading state. This is because, the lateral extension along the S-direction (i.e. global z-direction) is easier compared to that along the T-direction (i.e. global x-direction); in fact, extension along the T-direction stagnates while that along the S-direction evolves rapidly in the initial, twinning-dominated regime of plasticity. Once twinning is complete, the $\langle c \rangle$ -axis gets distributed in the LT-plane, which results in a decrease in the rate of extension along the S direction and a concomitant increase in the rate of extension along the T-direction and hence, $R_L^C \rightarrow 1$. In the twinning regime ($E_{eq} \leq 0.065$), sharper the texture the more negative (and hence, more anisotropic) the lateral strain ratios R_L^C and R_T^C . Interestingly, weaker textures exhibit a stronger deformation anisotropy beyond the twinning regime ($E_{eq} \gtrsim 0.065$). With decreasing basal peak strength, as in cases J and K, lateral deformation anisotropy decreases, but the tendency of R_L^C (and R_T^C) to go closer to 1 is much lesser than in S-tension and the strain dependency of R in twinning–post twinning regimes is still apparent.

Figs. 4c, 4f provide details of the texture-dependent variability of the deformation mechanisms for L- and T- compressive loading, respectively. In the post-twinned regime, the variability of the deformation activity is much tempered compared to the S-tension. It explains the lower variability in their post-twinning hardening compared to S-tension. The lower variability of $\bar{\xi}^i$ in L- (or T-) compression compared to its counterpart in S-tension arises from the fact that in the latter more twin variants are operative (cf. Fig. 8). We note that in both loading orientations, the overall $f^{\rm ET}$ (shown in the inset) is similar and comparable to the S-tension case

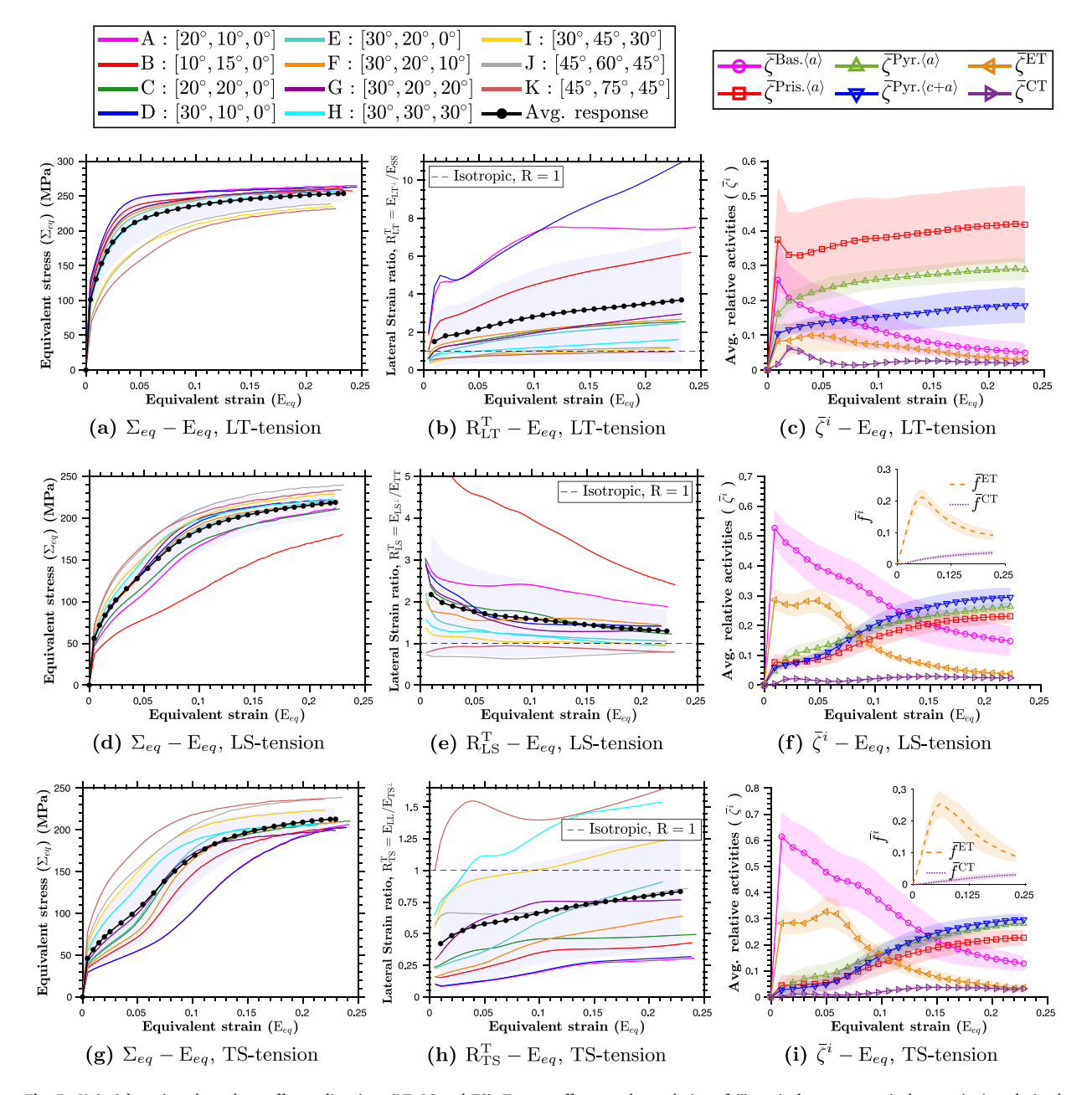


Fig. 5. Uniaxial tension along three off-axes directions (LT, LS and TS). Texture effects on the evolution of (i) equivalent stress-equivalent strain (panels (a, d, g)), (ii) lateral strain ratio (panels (b, e, h)), and (iii) relative activities of deformation mechanisms (panels (c, f, i)).

Compressive loading along the S-direction (Fig. 4g) is slip-dominated and hence, may be compared against tensile behaviors along the L- and T-directions. Unlike the L- and T-tension, textural variability has a pronounced effect on the compressive stress–strain response along the S-direction. Group-1 (lower Φ^{σ}) textures exhibit some of the strongest behaviors while Group-4 and Group-5 textures (large Φ^{σ} and φ_2^{σ}) produce the weakest responses. Note that in all cases (except case G), $R_S^C < 1$ over the entire deformation range. Moreover, the deformation anisotropy is larger ($R_S^C \ll 1$) for larger Φ^{σ} (cf. Group-1 and Group-2), which is not expected. However, when the textural weakening due to higher Φ^{σ} is compounded by the increased deviation in φ_2^{σ} , it tends to become less anisotropic.

Fig. 4i quantifies the sensitivity of deformation mechanisms to textural variations. Sharper initial textures exhibit much higher pyramidal $\langle c+a\rangle$ slip activity compared to weaker initial textures — a consequence of the Schmid effect. We note that, in case A, $\bar{\zeta}^{\langle c+a\rangle} \approx 0.9$ at $E_{eq} = 0.10$, whereas in case H, it is only. ~ 0.4 at the same strain level. The decrease in $\bar{\zeta}^{\langle c+a\rangle}$ by virtue of a weaker texture is compensated by increased basal $\langle a \rangle$ slip activity. In other words, weakening of initial texture causes enhanced basal $\langle a \rangle$ slip

activity in the material, which results in texture-induced softening of both, the flow stress and the hardening-rate, similar to experimental observation on strip-cast AZ31 alloy sheets with weak basal texture (Lee et al., 2011). Interestingly, for weaker initial textures (i.e. cases J and K), extension twinning becomes a non-negligible deformation mechanism and this results in a mild but perceptible inflection in stress–strain response which is similar to L- and T- compression responses for these textures. The relative activity plot also explains the fact that $R_S^C < 1$ (except case G); any shear strain accrued on the predominant pyramidal $\langle c + a \rangle$ slip system has a higher component along the S direction than in the LT plane. But with larger Φ^σ the basal $\langle a \rangle$ slip activity adds to the strain contribution in LT plane, thereby reducing the lateral strain anisotropy ($R_S^C \to 1$). With textural weakening the R_S^C evolution resembles R_S^C (and R_S^C).

3.3. Off-axes tensile and compressive responses

Figs. 5 and 6 respectively collate the tensile and compressive responses, as a function of the initial texture, for three off-axes loading orientations: LT, LS and TS, which are at 45° to the principal directions. As in the preceding section, the average response and the standard deviations are also shown in the plots.

On the backdrop of the observations from the previous section, some of the salient features are highlighted here. First, tensile loading along LT plane produces responses that are very similar to L (and T). Interestingly though, the textural effect is much tempered in this case compared to the variability seen in the L and T tension, particularly at high strains (cf. Fig. 5a). The reason can be related back to the origins of variability in the L and T cases. It so turns out that the mechanisms that cause variability in L-tension tend to negate the variability in T-tension, and vice-versa. Thus, a specimen loaded in tension along LT tends to inherit these effects from both the limiting cases resulting in a lower variability. Seen differently, the lower variability in LT-tension results from smaller differences between the resolved stresses along individual variants of prismatic $\langle a \rangle$, pyramidal $\langle a \rangle$ and pyramidal $\langle c + a \rangle$ slip modes than in L (or T). With increasing textural randomization, the variability would further reduce. The magnitude and variation of R_{LT}^{C} as a function of texture (cf. Fig. 5b) also is very similar to cases L and T. LT-compression exhibits a sigmoidal response (cf. Fig. 6a) with similar deviations and textural effects as seen in L- and T-compression. The trends in the evolution of R_{LT}^{C} are consistent with those in L (and T) compression, which include: (i) transition of $R_{LT}^{C} < 0$ in the twinning-dominated regime to $R_{LT}^{C} \rightarrow 1$ in the post-twinned regime, and (ii) an anomalous increase in the deformation anisotropy in the post-twinned regime with increasingly weaker initial texture (cf. Fig. 6b).

The tensile (cf. Figs. 5d, 5g) as well as the compressive (cf. Figs. 6d, 6g) stress–strain responses along the LS and TS directions vary systematically with textural variation — from sigmoidal (sharper texture, case A) to power-law form of hardening (weak texture, cases H–K), similar to S-tension. The tension–compression asymmetry is dramatically lower along these off-axes directions, which corroborates with experiments (Kondori et al., 2018). Interestingly, for both LS and TS orientations, weaker initial textures exhibit stronger tensile as well as compressive responses. It stands in contrast to the observation in the principal-axes loading cases where weaker initial textures produced weaker responses. Note that textural variability has a larger effect on the flow stress along the TS-direction compared to the LS-direction, while the strain ratios are more sensitive to textural effects in the LS-direction than the TS-direction, in both tension and compression.

Yet another interesting observation is that φ_1^σ (which had a negligible effect on L, T, S and LT responses) plays a dominant role in the LS behavior under both, tension and compression. For instance, consider the paired cases: (A, D) and (C, E), cf. Figs. 5d and 6d. For a constant $\Phi^\sigma=10^\circ$, increasing φ_1^σ (case A: $\varphi_1^\sigma=20^\circ$; case D: $\varphi_1^\sigma=30^\circ$) raises the flow stress while also reducing the lateral deformation anisotropy (R_{LS}^T) with a similar trend for $\Phi^\sigma=20^\circ$ (cases C and E). Moreover, the relative increase in the flow stress (at a given strain) between cases A and D is similar in magnitude to that between cases C and E. On the other hand, the relative decrease in R_{LS}^T between cases C and E is smaller than between cases A and D. Similar observation can be made for the pairs (H, I) and (J, K) possessing similar φ_1^σ . In other words, a smaller Φ^σ renders a stronger effect in reducing the deformation anisotropy compared to φ_1^σ . We note in passing that increasing φ_2^σ has a smaller positive effect on the flow stress with a corresponding lowering of the deformation anisotropy (cf. cases F and H).

The relative activity plots for the LT cases follow trends that are similar to the L and T cases, and are not discussed further for brevity.

In TS-tension (cf. Fig. 5g) a weaker initial texture enhances flow stress (as in the LS-tension case), although it is associated primarily with the variability of Φ^{σ} than φ_1^{σ} . Using the Groups defined in the preceding section, we find that Group-1 (A,D,B) exhibits the weakest flow stress and the most anisotropic deformation, followed by Group-2 (C,E) and Group-3 (F,G). Group-4 (H, I) and Group-5 (J, K) exhibit the strongest flow stress with an increasingly power-law type behavior and the lowest deformation anisotropy, particularly at large strains.

The LS and TS stress responses exhibit a much milder tension–compression asymmetry compared to other orientations with regards to its dependence on the initial texture. On the other hand, the asymmetry in the lateral deformation anisotropy ratios is relatively large.

From a mechanisms viewpoint, TS-tension produces more extension twinning than the LS counterpart, which explains difference in the flow stress between the two cases. In compression, there is slightly less extension twinning compared to their tensile counterparts. Moreover, textural variability induces a competition between the rate of decrease in the basal $\langle a \rangle$ slip and a concomitant increase in the pyramidal $\langle c+a \rangle$ slip. The latter increases with increased textural randomization (weaker textures) and is responsible for the enhanced flow stress and decreased lateral deformation anisotropy. Broadly speaking, the rate of decrease in $\bar{\zeta}^{\rm ET}$ (a reflection of the rate of reorientation) is a function of the initial texture — it is more rapid in a weaker texture (e.g. case H). Interestingly, it also appears to corroborate with the basal $\langle a \rangle$ slip and non-basal (prismatic $\langle a \rangle$ and pyramidal $\langle c+a \rangle$) slip rates of relative activities.

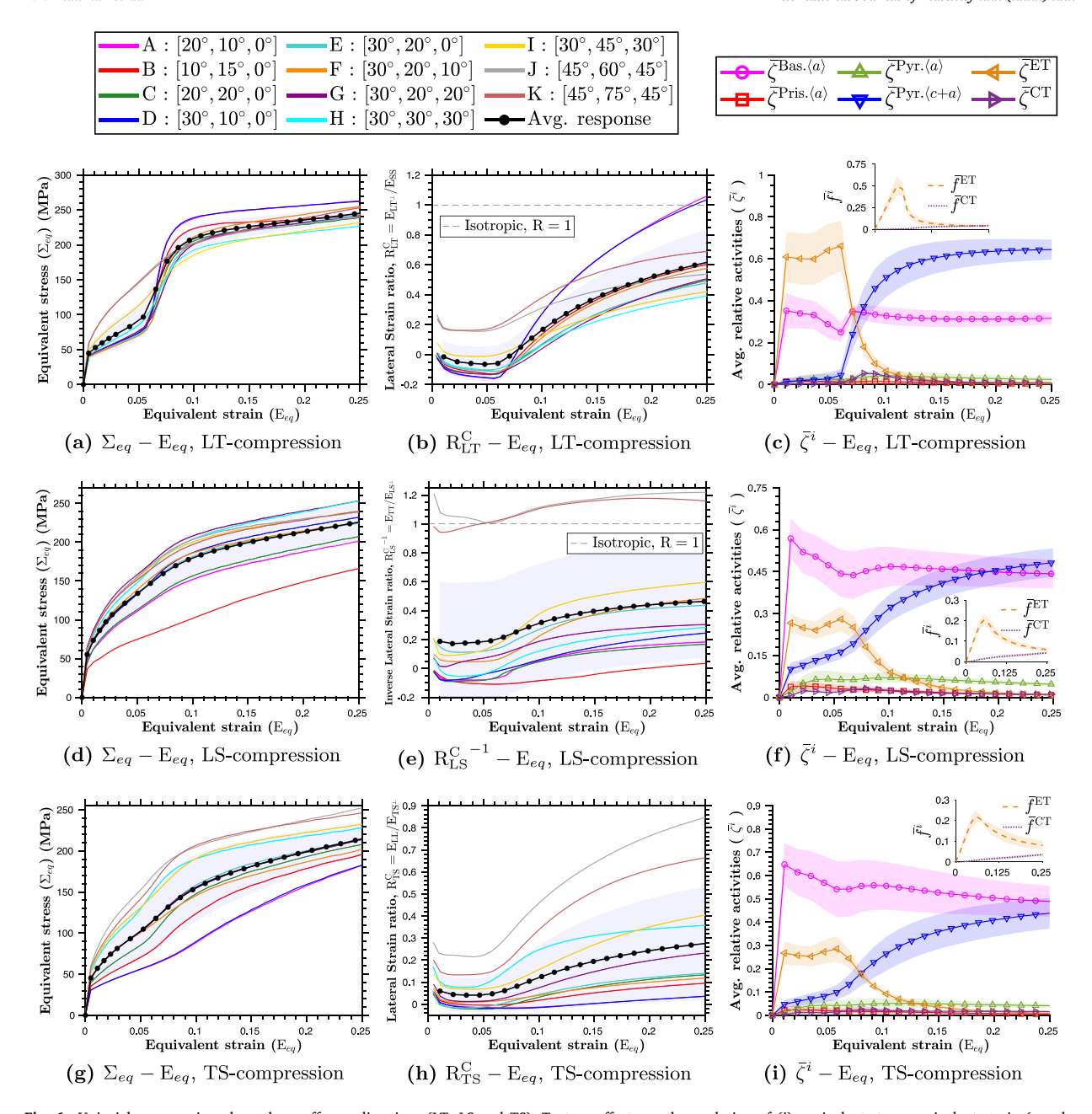


Fig. 6. Uniaxial compression along three off-axes directions (LT, LS and TS). Texture effects on the evolution of (i) equivalent stress-equivalent strain (panels (a, d, g)), (ii) lateral strain ratio (panels (b, e, h)), and (iii) relative activities of deformation mechanisms (panels (c, f, i)).

3.4. On the effect of crystallographic anisotropy

To understand the effect of intrinsic crystallographic anisotropy (at the single crystal scale) on the polycrystalline texture-property linkages, we performed identical set of simulations using the material parameters with a overall larger crystallographic anisotropy, representative of pure Mg (Table 4). Details aside, we note that the trends for polycrystalline pure Mg broadly follow those reported here for the AZ31 alloy. Interestingly, relative to the AZ31 case the macroscopic deformation anisotropy and its variability, both are rather sensitive to textural variations in pure Mg. For brevity, we omit a detailed presentation of the three-dimensional plastic anisotropy but discuss its potential role in damage. For more details on pure Mg results, the reader is referred to Indurkar et al. (2020) and Supplementary Material (Section S-4).

Table 5 Effect of weakening texture (going from case A to case K) on the strength (Σ_{eq}) and lateral deformation isotropy (\mathcal{L}) and microscopic activities - $\bar{\zeta}^{\text{soft sl.}}$, $\bar{\zeta}^{\text{hard sl.}}$ and $\bar{\zeta}^{\text{twin}}$. The observations are reported at two nominal strain levels (5% and 20%).

| Direction | Stress Strength ${\cal L}$ $ar{\zeta}^{ m soft \ sl.}$ | | | $\bar{\zeta}^{ m hard}$ sl. | | $ar{\zeta}^{	ext{twin}}$ | | | | | |
|-------------|--|----|-----|-----------------------------|-----|--------------------------|----------|----|-----|----|-----|
| | | 5% | 20% | 5% | 20% | 5% | 20% | 5% | 20% | 5% | 20% |
| L, T and LT | Tens. | | 7 | , | 7 | , | 7 | | \ | | 1 |
| | Comp. | 1 | 7 | 7 | 7 | , | <i>7</i> | 1 | 7 | > | 1 |
| c | Tens. | 1 | 7 | , | 7 | , | 1 | 1 | 7 | > | 1 |
| 3 | Comp. | | 7 | 7 | 7 | , | 7 | | 7 | | 1 |
| LS | Tens. | | 7 | , | 7 | ` | 7 | | 1 | | 7 |
| LS | Comp. | | 7 | , | 7 | ` | 7 | | 1 | | 1 |
| TS | Tens. | | 7 | , | 7 | , | 7 | | 1 | 1 | 7 |
| | Comp. | | 7 | , | 7 | ` | 7 | | 1 | 1 | 7 |

4. Discussion

As noted in the Introduction, there exists a body of experimental and modeling literature on the macroscopic behaviors of hexagonal materials. On that backdrop, an emphasis of the present work is on laying out a systematic map of the texture-property linkages in hexagonal materials using Mg as a model material. We note here that the results presented in the preceding sections (particularly for alloyed Mg) broadly corroborate with a range of experimental reports, although it is difficult to establish a precise quantitative corroboration due to experimental variations. It is in this regard that the present work provides a basis for a systematic understanding. We first present a brief comparison with some of the experiments available in the literature but note that the present work enables deeper insights beyond these broader comparisons, discussed in the subsequent sections.

A survey of in-plane (LT plane) experimental datasets for AZ31 and other Mg alloys (Lou et al., 2007; Bohlen et al., 2007; Khan et al., 2011; Tari et al., 2014) confirms a good qualitative corroboration of the simulated responses with the following observations: (i) a higher tensile flow stress and larger strain anisotropy along the T-direction compared to the L-direction, (ii) increasing deformation anisotropy with tensile strain along the L-, T-, and LT-directions; (iii) smaller initial overall deformation anisotropy in compression along the L-, T-, and LT-directions. (iv) a higher strength and hardening rate in S-compression compared to tension along L (and T) (i.e. for similar deformation mechanisms).

Likewise, for the out-of-plane (TS and LS planes) results, the simulations broadly assert experimental observations (Wang and Choo, 2014; Guo et al., 2015; Kondori et al., 2018): (i) transition from a sigmoidal to a power-law type behavior of the tensile responses traversing from 0° to 90° starting from the S-direction, (ii) enhanced sigmoidal behavior in the compressive responses traversing 0° to 90° starting from the S-direction in the TS plane, and (iii) dominant basal $\langle a \rangle$ slip activity in both, tension and compression, along the loading orientations spanning 30° to 60°) in the TS and LS planes. Finally, the consistent variation of f^{ET} as a function of the loading orientation along LS and TS plane is also captured (discussed *et seq.* in Section 4.1).

We also note that the textural variability effect on the hardening rate, lateral deformation anisotropy, and twinning broadly corroborate with prevalent observations (Lee et al., 2011; Wang et al., 2010).

4.1. On interplay between loading orientation and textural variation

Table 5 summarizes the overall effect of textural weakness (going from case A to case K) under different loading scenarios on macroscopic strength and lateral deformation isotropy (measured by $\mathcal{L}=|1-R|$) and consolidated deformation activity: $\bar{\xi}^{\text{soft sl.}}=\bar{\xi}^{\text{basal}}, \; \bar{\xi}^{\text{hard sl.}}=(\bar{\xi}^{\text{prism}}+\xi^{\text{pyr.}\langle a\rangle}+\bar{\xi}^{\langle c+a\rangle})$ and $\bar{\xi}^{\text{twin}}=(\bar{\xi}^{\text{ET}}+\bar{\xi}^{\text{CT}})$. An "up" ("down") arrow indicates that the particular quantity increases or becomes better (decreases or becomes worse) as the initial textural strength decreases.

The effect of textural variability on the evolution of strength asymmetry and plastic anisotropy is further evaluated by performing simulations along multiple off-axes loading cases in the LS and TS planes. For brevity, we present the results for three representative initial textures: Case A (sharp), case E (intermediate), and Case H (weak). Case K is marked by near isotropic responses and not included here for brevity. An off-axis loading is defined by angle θ that measures the deviation of the loading direction from a principal direction - L (in the LS plane) and T (in the TS plane). Fig. 7 consolidates the responses at fixed strain levels as a function of θ and demonstrates corroboration with some of the most comprehensive experimental datasets. The reader is referred to Supplementary Material (Section S-3) for more details on the results for LT plane and the corresponding micromechanical analysis.

Figs. 7a–7b show the flow stresses as a function of θ in the two planes. For the weak (case H) and intermediate (case E) textures, the tensile and compressive flow stresses exhibit a quasi-linear dependence on θ . Immediately following the initial yield ($E_{eq} \sim 1\%$), the strongest and the weakest tensile responses respectively correspond to $\theta = 0^{\circ}$ and $\theta = 90^{\circ}$, and the reverse is true for the compressive responses. On the other hand, for an initially sharp texture (case A), the flow stresses are non-monotonic with respect to θ ; the weakest compressive and tensile responses correspond to $30^{\circ} \lesssim \theta \lesssim 45^{\circ}$. With increasing deformation, the strength asymmetry and anisotropy tends to decrease, and the reduction is most discernible for the LS and TS orientations (i.e. $\theta = 45^{\circ}$).

In tension, the flow stress initially evolves due to enhanced basal $\langle a \rangle$ slip activity as θ increases from 0° to $\sim 45^{\circ}$ while it is the ET activity that governs the behavior for θ increasing beyond 45° to 90° , both being relatively soft mechanisms. Of course, their importance relative to the harder non-basal modes depends on texture. Weaker initial textures tend to negate extreme effects and

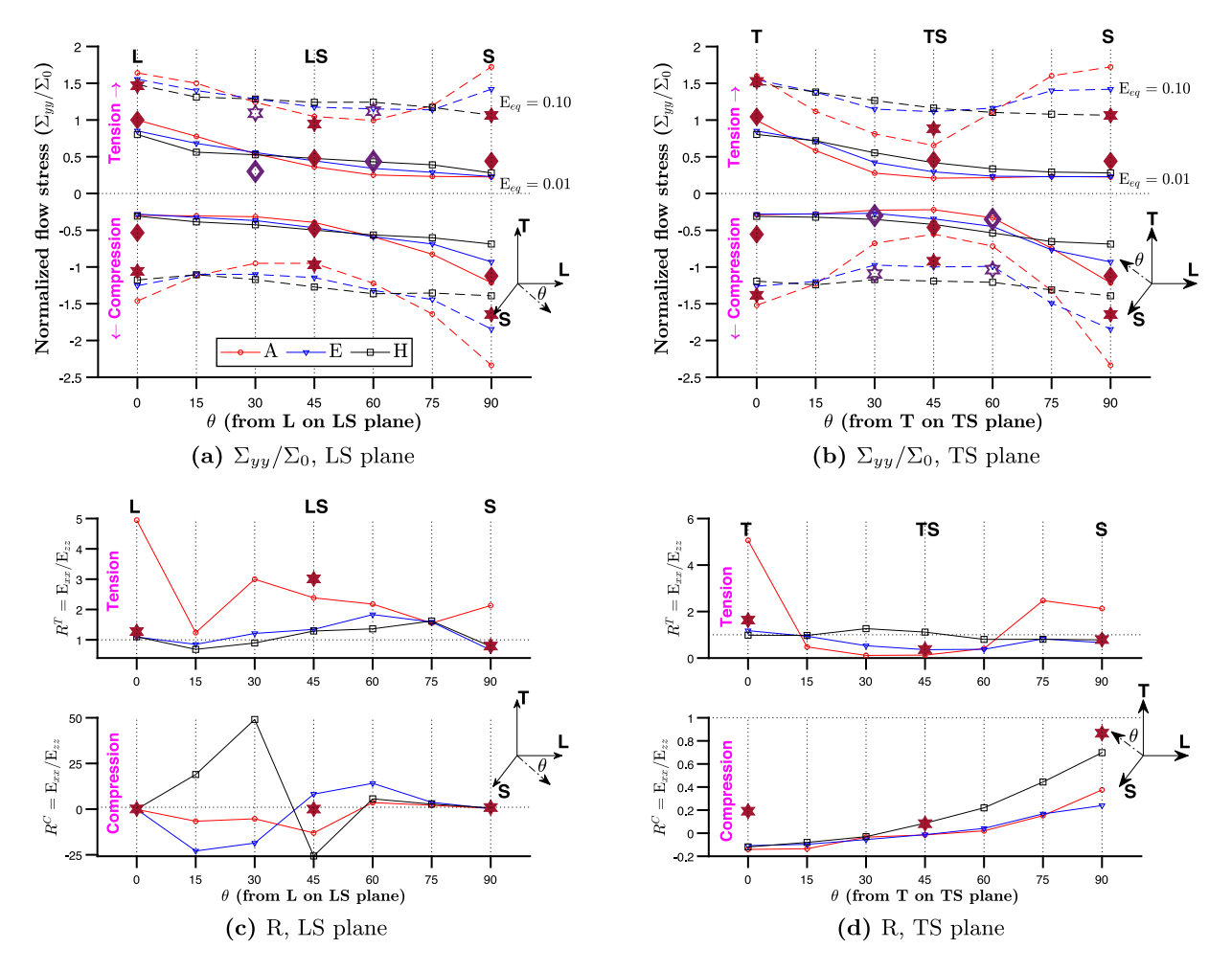


Fig. 7. A map of normalized stress anisotropy and asymmetry evolution (Panels a, b) and lateral strain ratio (Panels c, d), R as a function of θ in the LS and TS planes. In panels (a) and (b), \spadesuit and \star symbols are experimental results from Kondori et al. (2018) and \diamondsuit ($E_{eq} = 1\%$) and \star ($E_{eq} = 10\%$) are from Guo et al. (2015) at the corresponding strain levels. Σ_0 is the tensile stress in the L-direction for case A at $E_{eq} = 1\%$. Likewise, the experimental results are normalized by their tensile stress in the L-directions. In panels (c) and (d), the simulation and experimental (\star , Kondori et al., 2018) results are at $E_{eq} = 5\%$.

as a result, their responses are less sensitive to θ compared to those for the initially sharper textures. At larger strains, the initial effect of the soft modes sets the flow stress levels, particularly when extension twinning is the initial governing mechanism. These trends reverse for the compressive loading state.

Figs. 7c and 7d indicate that the lateral deformation anisotropy dependence on θ is complicated by textural variations. The responses are non-monotonic, but it is difficult to generalize the interacting role of texture and loading. For instance, case H (weak texture), which exhibits a relatively isotropic deformation behavior over the entire range of θ , shows a rather complicated anisotropic behavior in compression.

4.2. On the coupling between deformation mechanisms and texture evolution

The evolution of pole figures provides additional insight into the interaction between the deformation mechanisms and texture evolution. For brevity, the pole figures are relegated to Supplementary Material (Section S-5), but the key aspects are discussed here.

In slip-dominated scenarios (e.g. L-, T-, LT-tension or S-compression), initially sharper textures suffer from exacerbated textural weakening over the same strain range compared to their weaker counterparts. The accelerated textural weakening is a consequence of more rapid evolution of the lattice rotation due to higher non-basal slip (prismatic $\langle a \rangle$ slip and pyramidal $\langle c + a \rangle$ slip) resulting from the texture induced asymmetry between their individual variants as a function of the loading direction. Between these scenarios, L-tension promotes more textural weakening of [10 $\bar{1}$ 0] compared to [0001] (higher prismatic $\langle a \rangle$ slip) while S-compression promotes more textural weakening of [0001] compared to [10 $\bar{1}$ 0] (higher pyramidal $\langle c + a \rangle$ slip). In both these scenarios no perceptible pole shifting/splitting occurs. Off-axes out-of-plane loading (e.g. TS-tension and compression) also favor basal $\langle a \rangle$ slip slip activity

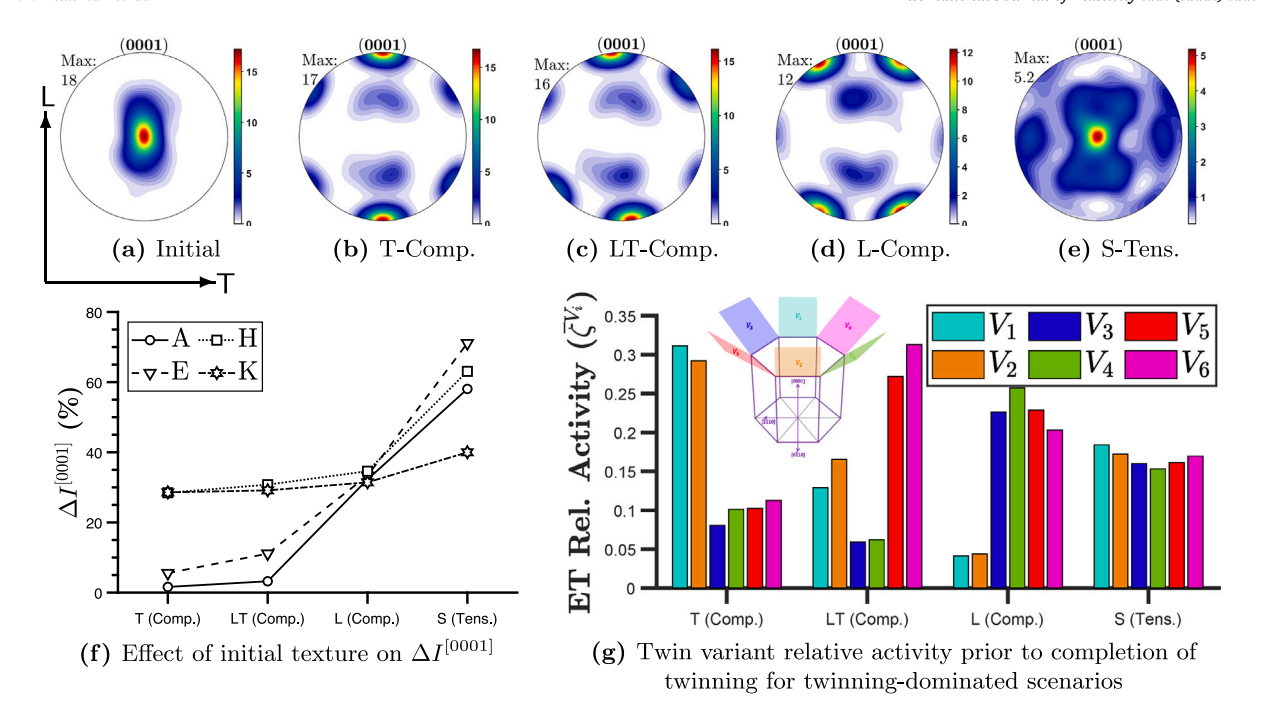


Fig. 8. Panels (a)–(e) show the representative (for case E) initial and deformed [0001] pole figures projected on the LT plane for T-, LT-, L- compression and S-tension respectively at $E_{eq} = 0.10$. Panel (f) shows the effect of initial texture on % change in $\langle c \rangle$ -axis intensity ($\Delta I^{[0001]}$) at 10% strain arising due to probabilistic twin-variant selection as a function of loading direction/state as shown for texture E in Panel (g). $V_1:(0\bar{1}12)$ [01 $\bar{1}1$], $V_2:(01\bar{1}2)$ [0 $\bar{1}11$], $V_3:(1\bar{1}02)$ [101], $V_4:(1\bar{1}02)$ [101], $V_5:(10\bar{1}2)$ [101] and $V_6:(10\bar{1}2)$ [101].

with moderate extension twinning ($f^{\rm ET}\sim30\%$). As a result, in these orientations the deformation-induced textural weakening is accompanied by pole shifting and splitting. Also, the accrued twin volume fraction is a non-monotonic function of the initial texture strength; at $E_{eq}=5\%$, textures A, E and H respectively accrue $f^{\rm ET}\sim18\%$, 29% and 22% respectively, while the corresponding reductions in the textural intensity of the [$10\bar{1}0$] pole figures is $\sim8\%$ (case A), 24% (case E) and $\sim5\%$ (case H), respectively.

Consider four twinning-dominated loading cases: S-tension, L-compression, T-compression, and LT-compression. In each of these, the average maximum extension twin volume fraction, $f_{\rm ET} \sim 0.55-0.60$. Yet, for the same starting texture, they show very different textural evolution, Figs. 8a–8e. An instantaneous change in texture occurs upon twinning marked by the pole shifting and splitting in the [0001] pole figures, except in S-tension. From the standpoint of controlling the plastic anisotropy, this raises two fundamental questions (Hong et al., 2010)–(i) what role does loading orientation play in the coupling between twinning and textural evolution? and (ii) how does textural variation affect this coupling? To that end, Fig. 8f shows the % change in the peak textural intensity ($\Delta I^{[0001]}$) relative to the initial peak texture intensity for the four twinning-dominated loading orientations and three representative initial textures (at a fixed strain $E_{eq}=0.1$). Note the dramatic increase in $\Delta I^{[0001]}$ going from the T-compressive to the S-tensile loading state. The trend is consistent for the range of textures and can be directly related to the twinning variant relative activity in each loading case for a given texture (case E is illustrated in Fig. 8g). S-tension promotes nearly equal activation of each variant, which creates an equal probability for the grains to take up any of the six twinned orientations. By way of consequence, texture randomization ensues, which results in a large change in $\Delta I^{[0001]}$ (textural weakening). At the other end of the spectrum, T-compression activates only two twin variants (LT-compression also shows a similar behavior), which has a minor effect on the peak deformed textural intensity. The intermediate case of L-compression is influenced by the activity of four twin variants, which gives rise to a moderate drop in the peak intensity.

In comparison to cases A (sharp texture) and E (intermediate texture), which experience a dramatic effect of the loading orientation on the textural evolution through the choice of twinning variants, case H (a weak texture) presents a more equable effect of the loading orientation on the textural variation (cf. Fig. 8f). In other words, loading orientation has a stronger effect on twinning induced textural evolution in microstructures with initially sharp to intermediate textures. For extremely weak textures (case K) where the net extension twinning activity is low, individual twin variants do not play a major role in the texture evolution as a function of the loading orientation (cf. Fig. 8f). A detailed Schmid-based reasoning for this preferential activation and evolution of variant activity can be found in Supplementary Material (Section S-5).

Efforts at formulating improved reduced-order models of hexagonal metal plasticity (such as Steglich et al., 2016; Kondori et al., 2018; Becker and Lloyd, 2016) should benefit from the foregoing observations. In particular, the sensitivity of textural coupling into the orientation-dependent material response indicates the need to distinguish between the soft and hard modes of slip-driven plasticity in addition to twinning-affected plasticity (cf. Table 5).

4.3. On the role of twinning in macroscopic anisotropy

In contrast to slip-dominated responses (e.g. tension along L, T (Figs. 3b–3e), compression along S (Fig. 3h)) where weaker textures temper the lateral deformation anisotropy (i.e. $R \rightarrow 1$), the twinning dominated responses (e.g. compression along L, T (Figs. 4b–4e), LT (Fig. 6b)) exhibit more pronounced deformation anisotropy for initially weaker textures as R drops below unity for initially weaker textures, i.e. sharper textures provide more isotropic deformations. Insofar as designing the plastic anisotropy via textural control, such a dichotomy presents a challenge.

Also noteworthy is the *transient plastically auxetic* behavior, which indicates the tendency of the material to contract along a lateral direction when compressed along the primary direction. The negative R_L^C , R_L^C , R_L^C , and R_{LS}^C ratios (Figs. 4b, 4e, 6b, and 6e) reveal that such a phenomenon can occur for different compressive loading states but not under tensile loading at least in Mg. A similar phenomenon has been reported in experiments (Chun and Davies, 2011; Zhou et al., 2016; Kondori and Benzerga, 2014) under L-compression. Its persistence in the initial regime shortly after yield is a consequence of extension twinning when subjected to compression perpendicular to the c-axis. Indeed, the theoretical underpinnings relate to the c/a ratio being smaller than $\sqrt{3}$ which promotes this twinning induced phenomenon under the particular compressive loading states (Chun and Davies, 2011; Zhang and Joshi, 2012). On that backdrop, the current work reveals several additional salient features — (i) it can be observed under loading orientations other than just the L-compression including T, LT- and LS-compression, (ii) the range of textures for which it occurs depends on the loading orientation (cf. Figs. 6b versus 6e), which emphasizes the sensitivity of deformation anisotropy to textural variations, and (iii) certain textures may produce little to no lateral deformation in that regime (e.g. case I in L-, T-, and LT-compression and case H in LS-compression) and these are transitional textures beyond which any further initial textural weakening will suppress the auxetic behavior.

A closer examination of R_L^C (also R_L^C and R_{LT}^C) responses for cases J and K hints at potential approaches to mitigate the constraints in achieving lateral deformation isotropy under L (also T and LT) compression. For instance, by introducing pre-twinned microstructures (Lloyd et al., 2020) the initial low R values in the twinning regime could be effectively compensated by creating a more directionally equable straining during early stages of deformation.

Finally, the remarkable variability of the flow stress evolution in the twinning-dominated orientations is a direct consequence of the sensitivity of twinning to textural variation. Two canonical flow stress evolution trends can be observed due to this coupling. In the first, textural variability affects the final saturation strength (after twinning is complete) while the flow stress during twinning evolution remains relatively unaffected (cf. Fig. 3g). In the second, texture modulates the twinning-affected hardening behavior while having a negligible effect on the final saturation strength (cf. Fig. 5g). Recent micromechanical calculations (Selvarajou et al., 2019; Indurkar and Joshi, 2019) indicate that such variations may have a potent effect on damage accumulation rates in hexagonal materials.

4.4. Implications on failure

The foregoing results correlate the textural variability to the variability in the anisotropic responses. A logical extended question is: can we make projections from these damage-free responses on the damage tolerance of hexagonal materials? In ductile materials, one of the two modes of failure may prevail (Pineau et al., 2016) — (i) internal damage accumulation by void evolution, or (ii) shear instability. For the former, Basu et al. (2017) invoked the notion of a scalar metric — AED (anisotropy effect on ductility) index, while the latter has been shown to depend on the material shear anisotropy ratios (Benzerga et al., 2019). Both these metrics invoke a micromechanical basis of Hill's quadratic yield anisotropy (Hill, 1948). Recent experimental (Nemcko et al., 2016b,a; Prasad et al., 2018) as well as computational efforts (Selvarajou et al., 2019; Kondori and Benzerga, 2017; Prasad et al., 2016; Indurkar and Joshi, 2019) indicate that microstructural aspects of hexagonal materials play a more critical role in their damage evolution compared to materials with higher crystal structure symmetry. Admittedly, in such materials the Hill model may appear to be somewhat simplistic. Nevertheless, a major advantage of the Hill model is that the anisotropy coefficients are physically meaningful. As such, it provides a practical basis to make engineering interpretations of the anisotropy effect on failure. While other measures of plastic anisotropy exist, their parametrization may render physical insights that are difficult if not impossible (Cazacu and Barlat, 2004; Stewart and Cazacu, 2011), or are somewhat restrictive (Kumar et al., 2017) to make broader connections with the damage tolerance as a function of the initial microstructure. Motivated by recent promising explorations (Basu et al., 2017; Benzerga et al., 2019), we adopt the Hill anisotropy principles to assess the potential effect of textural variability on the mode of damage in hexagonal materials.

The AED index (h) is a scalar invariant of the Hill tensor h (Benzerga and Besson, 2001; Keralavarma and Benzerga, 2010):

$$h = 2\left[\frac{2}{5}\frac{h_{\rm L} + h_{\rm T} + h_{\rm S}}{h_{\rm L}h_{\rm T} + h_{\rm T}h_{\rm S} + h_{\rm L}h_{\rm S}} + \frac{1}{5}\left(\frac{1}{h_{\rm LT}} + \frac{1}{h_{\rm LS}} + \frac{1}{h_{\rm TS}}\right)\right]^{\frac{1}{2}}$$
(15)

where $h_{\rm L}, h_{\rm T}, h_{\rm S}$ are the coefficients of $\mathbb h$ along the principal material directions, and $h_{\rm LT}, h_{\rm LS}, h_{\rm TS}$ are those along the off-axis directions. Our focus here is on the tensile loading states for which the coefficients are computed as per (Basu et al., 2017) (see Appendix A for details). Fig. A.1 shows the evolution of the Hill coefficients for the simulated tensile dataset, which show a reasonable corroboration with some of the recent experimental observations.

Failure via internal damage accumulation by void evolution invokes the role of h, which governs void growth (Keralavarma et al., 2011). Micromechanics of void growth tells us that porosity evolution depends exponentially on 1/h (Benzerga and Besson, 2001), and hence, it has been recently termed as the AED index (Basu et al., 2017). Values of h > 2 delay porosity evolution

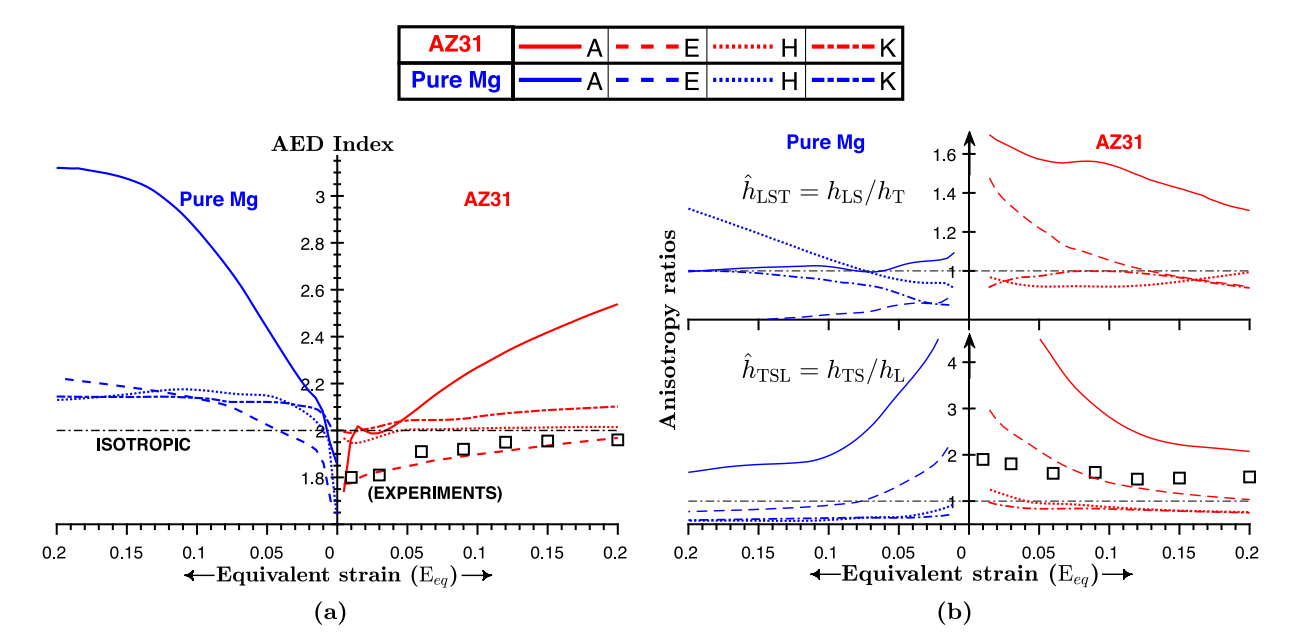


Fig. 9. Effect of initial texture on (a) the AED index h and (b) shear anisotropy ratios \hat{h} . Experimental results (shown as \square) are calculated from the AZ31 data given in Kondori (2015). Evolution of individual components of h is shown in Fig. A.1.

thereby increasing the strain to failure relative to their isotropic counterparts (h = 2). Likewise, h < 2 exacerbates porosity growth promoting early failure. On that backdrop, Fig. 9a shows the evolution of h for two different crystallographic anisotropies and four representative textures. Several interesting features emerge. For a given texture, pure Mg (larger crystallographic plastic anisotropy) is expected to perform better in terms of ductility compared to AZ31, its lesser anisotropic counterpart. Second, for a given material (pure Mg or AZ31), the AED index varies non-monotonically with texture strength. In other words, a weaker texture may not necessarily result in better resistance to internal damage accumulation. Cases K and H (weakest of the four textures) perform relatively better than case E (intermediate textural strength) but exhibits a poorer behavior than case A (strongest texture). Third, it appears that a material with larger crystallographic plastic anisotropy (pure Mg) is more forgiving to textural variations insofar as internal damage accumulation by void evolution is concerned compared to one with lower crystallographic plastic anisotropy (AZ31). Interestingly, this observation stands in good stead with the recent observations that a more anisotropic Mg alloy (AZ31) exhibits better tensile ductility than a less anisotropic Mg alloy (WE43) over a range of stress states (Kondori and Benzerga, 2014, 2015). Finally, larger the crystallographic plastic anisotropy the greater the variability in the AED index, which underscores the significance of textural variability in damage by void growth.

In the context of failure by shear bands, the shear anisotropy ratios: $\hat{h}_{TSL} = h_{TS}/h_L$, $\hat{h}_{LST} = h_{LS}/h_T$ are of interest. They depict the propensity to shear instabilities in TS and LS planes, respectively. We note that $\hat{h} > 1$ indicates a material that is weak in shear whereas $\hat{h} \le 1$ indicates a shear-resistant material (Benzerga et al., 2019). Fig. 9b shows the evolution of \hat{h} ratios for pure Mg and AZ31 Mg alloy. Both materials present a complicated dependence on texture. Case A (strongest texture) shows a propensity to shear banding in both materials. On the other hand, there is a degree of textural dependence to the shear-resistant behavior determined by the condition $\hat{h}_{TSL} \le 1$ and $\hat{h}_{LST} \le 1$. Cases E and K for pure Mg and Cases H and K for AZ31 exhibit such a characteristic. Pure Mg shows a shear-resistant behavior in both planes in the early stages of plastic deformation ($E_{eq} \le 0.07$) for case H. However, with increasing deformation it becomes weak in shear in the LS-plane while remaining shear-resistant in the TS-plane. From these observations, we postulate that there exists a sufficiently weak texture, which is agnostic to the intrinsic crystallographic anisotropy insofar as the resistance to shear instability is concerned. As shown in the figure, the prediction for AZ31 bears a qualitative similarity with the experimental observations on axisymmetric round bars under uniaxial tension (Kondori and Benzerga, 2014).

These observations gleaned from mapping AED and \hat{h} with textures appear to corroborate with additional experimental observations, which show that the sheet limit strain increases with a decreasing intensity of the basal texture (Wang et al., 2010, 2011; Neil and Agnew, 2009). Such low basal intensity textures have also been shown to be less susceptible to shear bands (Gehrmann et al., 2005). A combined experimental–computational study on AZ61L alloys (Miller et al., 2016) concluded the basal peak intensity as the most important predictor of forming behavior. On that backdrop, our simulations show that in all but one scenarios, Φ^{σ} , which controls the basal peak intensity, plays the most critical role in the macroscopic behaviors. Only in the LS plane loading does this situation not hold. Moreover, the present work extends beyond the work of Miller et al. (2016) in that the effect of textural variations on the out-of-plane behavior are also accounted for.

While the qualitative comparisons of failure behavior with particular experiments are encouraging, the foregoing assessment goes further and predicts that the intrinsic crystallographic plastic anisotropy plays a role in the deciding which textures will perform

better against damage evolution. The following inferences may be made: (i) for both levels of plastic anisotropy, the strongest texture (case A) shows the highest resistance to void growth but also exhibits a strong susceptibility to shear instability, (ii) for materials with a lower plastic anisotropy, intermediate textures (e.g. case E) may be detrimental for both, void damage as well as shear banding. In such materials, a further weakening of initial textures (cases H, K) may be more beneficial against shear banding as well as void damage, and (iii) for materials with a higher crystallographic plastic anisotropy, intermediate textures (e.g. case E) show a better resistance to both, void growth and shear banding. In a broader sense, it appears that the subset of optimal textures for damage tolerant hexagonal materials may be narrowed by shear instability considerations.

5. Concluding remarks

In this work, we performed unprecedented three-dimensional, full-field crystal plasticity simulations comprising eleven textures, six loading orientations, two loading states (uniaxial tension and compression), and two material data sets, to extract texture-property linkages of technologically important hexagonal materials. The effect of textural variation and crystallographic anisotropy on the macroscopic anisotropic and asymmetric behaviors of hexagonal materials was laid out at various levels by relating them to micromechanical underpinnings. The extensive datasets generated in this work can potentially serve as a synthetic resource to calibrate and assess reduced order models of hexagonal plasticity. However, the work goes beyond a mere characterization exercise by making deeper connections between various micromechanical aspects of plastic anisotropy. Combining them with micromechanical principles of damage, we make projections of the textural variability on damage tolerance. Specific conclusions from this work are listed below:

- 1. Along material principal directions, slip-dominated tensile behaviors exhibit a stronger sensitivity to Φ^{σ} with φ_1^{σ} playing a secondary role. The variability of φ_2^{σ} seems to have a non-monotonic effect on the hardening as well as the strain anisotropy. In general, a stronger texture is also more anisotropic. In twinning-dominated tensile loading, twin hardening most strongly affected by Φ^{σ} . Strain anisotropy is more sensitive to textural variations but tend toward isotropy at larger strains. Weaker textures exhibit lower deformation anisotropy, however, intermediate textures present a favorable combination of material hardening and lower strain anisotropy.
- 2. Under compressive loading along the principal material directions, the slip-dominated responses are much more sensitive to textural variations. Deformation anisotropy increases with increasing Φ^{σ} but decreases with increasing ϕ_2^{σ} . For twinning-dominated loading, the strain anisotropy evolution is distinct from its tensile counterpart. While in the twinning regime the material is very stiff to lateral deformation (high anisotropy), anisotropy decreases with deformation, albeit at much slower rate compared to its tensile counterpart. Moreover, weaker textures exhibit a higher deformation anisotropy beyond the twinning regime. The plastic auxeticity can occur under a range of twin-friendly compressive loading states depending on the initial textural strength.
- 3. The tensile and compressive flow stress levels exhibit a non-monotonic dependence on the in-plane loading orientation, which is more discernible for sharper initial textures (at a given strain) and at larger strains for a given texture. Furthermore, the dependence of the lateral deformation anisotropy is also non-monotonic with the loading orientation but exhibits a complicated variation with texture. In twinning-dominated scenarios, for the same starting texture the textural evolution may be significantly different despite the overall twin volume fraction being similar, which is a result of the coupled effect between the texture and loading orientation. Intermediate and sharper textures may undergo a wide range of textural intensity evolutions relatively to their initial intensities, ranging between < 5% to > 50% depending on the loading orientation. On the other hand, weak textures may exhibit a large but relatively equable textural intensity changes by twinning across the same loading orientations.
- 4. Textural variations reveal a dichotomy with respect to the mechanism-dominated macroscopic plastic anisotropy. While weaker textures exhibit relatively isotropic lateral deformations under slip-dominated orientations, the same textures exhibit a strong deformation anisotropy under twinning dominated loading orientations. Furthermore, textural variations may either modulate the twinning-induced rate of hardening or the twinning-affected stress saturation. Such variations are expected to influence damage accumulation.
- 5. Engineering projections of damage tolerance based on micromechanical principles predict an intimate coupling between the intrinsic crystallographic plastic anisotropy and textural variations in the setting up ductility limits in hexagonal materials, particularly magnesium and its alloys. Results presented here suggest that hexagonal materials with higher crystallographic plastic anisotropy may be more tolerant to internal damage accumulation over a larger range of textural variations than those with lower crystallographic plastic anisotropy.

Declaration of competing interest

The authors declare that they have no known competing financial interests or personal relationships that could have appeared to influence the work reported in this paper.

CRediT authorship contribution statement

Padmeya P. Indurkar: Methodology, Software, Formal analysis, Visualization, Writing - original draft. Shahmeer Baweja: Methodology, Formal analysis, Data curation. Robert Perez: Methodology, Formal analysis, Data curation. Shailendra P. Joshi: Conceptualization, Methodology, Funding acquisition, Writing - review & editing, Supervision.

Table A.0 Anisotropy ratio expressions as a function of h_i and the simulation lateral strains mapped against these expressions (both L-T-S and x-y-z frames shown).

| Anisotropy ratio | Expression (Kondori, 2015; Basu et al., 2017) | L-T-S definition |
|------------------|---|---|
| R_L | $\frac{-2h_{\rm L} - 2h_{\rm T} + h_{\rm S}}{-2h_{\rm L} + h_{\rm T} - 2h_{\rm S}}$ | $\frac{E_{xx}}{E_{zz}} = \frac{E_{TT}}{E_{SS}}$ |
| R_T | $\frac{-2h_{\rm L} - 2h_{\rm T} + h_{\rm S}}{h_{\rm L} - 2h_{\rm T} - 2h_{\rm S}}$ | $\frac{E_{xx}}{E_{zz}} = \frac{E_{LL}}{E_{SS}}$ |
| R_{LT} | $\frac{18h_{\rm LT} - \left(h_{\rm L} + h_{\rm T} + 4h_{\rm S}\right)}{2\left(h_{\rm L} + h_{\rm T} + 4h_{\rm S}\right)}$ | $\frac{E_{xx}}{E_{zz}} = \frac{E_{LT^{\perp}}}{E_{SS}}$ |
| R_{LS} | $\frac{18h_{\rm LS} - \left(h_{\rm L} + 4h_{\rm T} + h_{\rm S}\right)}{2\left(h_{\rm L} + 4h_{\rm T} + h_{\rm S}\right)}$ | $\frac{E_{xx}}{E_{zz}} = \frac{E_{LS^{\perp}}}{E_{TT}}$ |
| R _{TS} | $\frac{2 \left(4 h_{\rm L} + h_{\rm T} + h_{\rm S}\right)}{18 h_{\rm TS} - \left(4 h_{\rm L} + h_{\rm T} + h_{\rm S}\right)}$ | $\frac{E_{xx}}{E_{zz}} = \frac{E_{LL}}{E_{TS^{\perp}}}$ |

Acknowledgments

SPJ acknowledges support provided by the National Science Foundation, USA under Grant Number CMMI-1932976. Partial support for PPI and SB was provided by the Army Research Laboratory, USA and was accomplished under Cooperative Agreement Number W911NF-12-2-0022. PPI acknowledges partial support from NUS Research Scholarship, National University of Singapore. RP acknowledges the Undergraduate Research Apprenticeship Program (URAP) Award under the Army Educational Outreach Program (AEOP). The views and conclusions contained in this document are those of the authors and should not be interpreted as representing the official policies, either expressed or implied, of the Army Research Laboratory or the U.S. Government. The U.S. Government is authorized to reproduce and distribute reprints for Government purposes notwithstanding any copyright notation herein.

Appendix A. AED index calculation

The AED responses in Section 4 are calculated using the strain-based method (Kondori, 2015; Basu et al., 2017) on macroscopic *tensile* data of textures A–H along directions L, T, LT, LS and TS¹ used in Sections 3.1 and 3.3. We equate the derived lateral strain ratio expressions from Hill48 (Hill, 1948) criterion (Table A.0) with corresponding strain ratios from our CPFEM simulations (see Table 2).

Using expressions in Table A.0, we solve simultaneously for h_L , h_T , h_S , h_{LT} , h_{LS} and h_{TS} as functions of R_L , R_T , R_{LT} , R_{LS} and R_{TS}^2 . Given that we fix our reference direction along L, not all 6 coefficients (h_i) are independent. Using normalized flow stress expression along L we get:

$$4h_{\rm L} + h_{\rm T} + h_{\rm S} = 6 \implies 4 + \left(\frac{h_{\rm T}}{h_{\rm I}}\right) + \left(\frac{h_{\rm S}}{h_{\rm I}}\right) = \left(\frac{6}{h_{\rm I}}\right) \tag{A.1}$$

Using expressions for R_L, R_T, R_{LT}, R_{LS} and R_{TS}, we get:

$$\frac{h_{\rm T}}{h_{\rm L}} = 1 - \frac{3\left(R_{\rm L}R_{\rm T} - 1\right)}{R_{\rm L}R_{\rm T} - 2R_{\rm L} - 2} \tag{A.2a}$$

$$\frac{h_{\rm S}}{h_{\rm L}} = 1 - \frac{3R_{\rm L} (R_{\rm T} - 1)}{R_{\rm L}R_{\rm T} - 2R_{\rm L} - 2}$$
(A.2b)

$$\frac{h_{\rm LT}}{h_{\rm L}} = -\frac{1}{2} \frac{\left(2R_{\rm LT} + 1\right)\left(R_{\rm L}R_{\rm T} + 1\right)}{R_{\rm L}R_{\rm T} - 2R_{\rm L} - 2} \tag{A.2c}$$

$$\frac{h_{\rm LS}}{h_{\rm L}} = -\frac{1}{2} \frac{\left(2R_{\rm LS} + 1\right) \left(R_{\rm L} + 1\right) R_{\rm L}}{R_{\rm L} R_{\rm T} - 2R_{\rm L} - 2} \tag{A.2d}$$

$$\frac{h_{\rm TS}}{h_{\rm L}} = -\frac{1}{2} \frac{\left(2R_{\rm TS} + 1\right)\left(R_{\rm L} + 1\right)}{R_{\rm L}R_{\rm T} - 2R_{\rm L} - 2} \tag{A.2e}$$

Using Eqs. (A.1) and (A.2), we solve for h_i (cf. Fig. A.1), which are then used to calculate AED (Anisotropy Effect on Ductility) also referred to as the scalar invariant of Hill anisotropy tensor (h), h (Benzerga and Besson, 2001; Keralavarma and Benzerga, 2010) Eq. (15).

Appendix B. Supplementary data

Supplementary material related to this article can be found online at https://doi.org/10.1016/j.ijplas.2020.102762.

 $^{^{\}mathrm{1}}$ Note that data lateral strain data along S was not required for this calculation.

² Note that the term R_S does not appear in h_i equations.

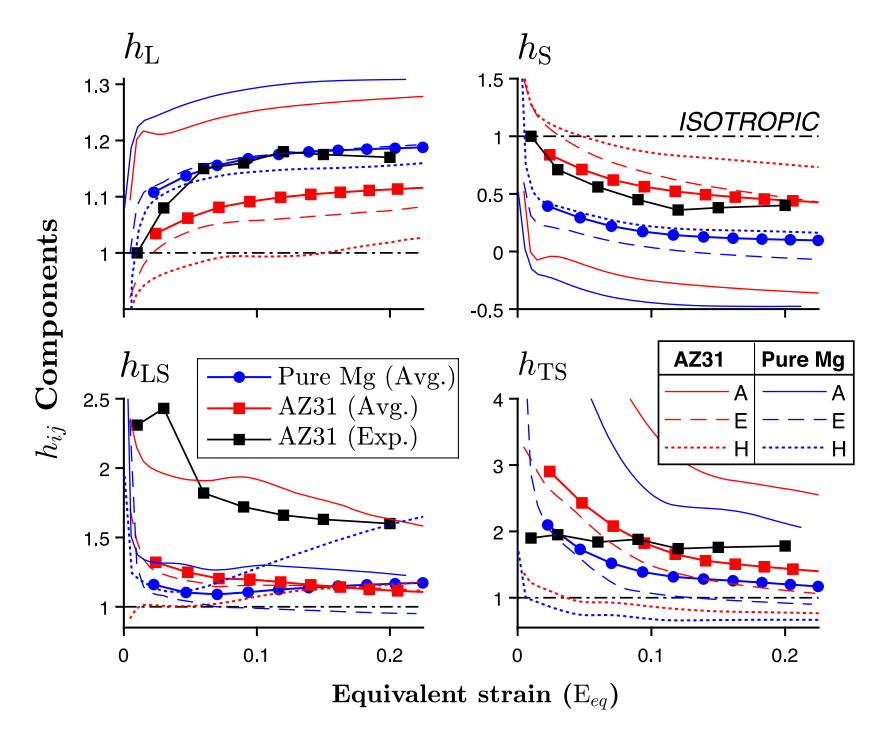


Fig. A.1. Evolution of h_i components mapped using strain-based method for tension simulations datasets compared with h_i components from experiments (Kondori, 2015). h_T and h_{LT} variations are similar to that of h_L and not shown for brevity.

References

Abdolvand, H., Daymond, M.R., 2013a. Multi-scale modeling and experimental study of twin inception and propagation in hexagonal close-packed materials using a crystal plasticity finite element approach - Part I: Average behavior. J. Mech. Phys. Solids 61 (3), 783–802.

Abdolvand, H., Daymond, M.R., 2013b. Multi-scale modeling and experimental study of twin inception and propagation in hexagonal close-packed materials using a crystal plasticity finite element approach - Part II: Local behavior. J. Mech. Phys. Solids 61 (3), 803–818. http://dx.doi.org/10.1016/j.jmps.2012.10.017, URL http://www.sciencedirect.com/science/article/pii/S0022509612002384.

Agnew, S., Brown, D., Tomé, C., 2006. Validating a polycrystal model for the elastoplastic response of magnesium alloy AZ31 using in situ neutron diffraction. Acta Mater. 54 (18), 4841–4852. http://dx.doi.org/10.1016/j.actamat.2006.06.020, URL http://www.sciencedirect.com/science/article/pii/S1359645406004502. Agnew, S.R., Duygulu, Ö., 2005. Plastic anisotropy and the role of non-basal slip in magnesium alloy AZ31B. Int. J. Plast. 21 (6), 1161–1193.

Agnew, S., Horton, J., Lillo, T., Brown, D., 2004. Enhanced ductility in strongly textured magnesium produced by equal channel angular processing. Scr. Mater. 50 (3), 377–381. http://dx.doi.org/10.1016/j.scriptamat.2003.10.006, URL http://www.sciencedirect.com/science/article/pii/S1359646203006687.

Agnew, S., Tomé, C., Brown, D., Holden, T., Vogel, S., 2003. Study of slip mechanisms in a magnesium alloy by neutron diffraction and modeling. Scr. Mater. 48 (8), 1003–1008.

Agnew, S., Yoo, M., Tomé, C., 2001. Application of texture simulation to understanding mechanical behavior of Mg and solid solution alloys containing Li or Y. Acta Mater. 49 (20), 4277–4289. http://dx.doi.org/10.1016/S1359-6454(01)00297-X, URL http://www.sciencedirect.com/science/article/pii/S135964540100297X

Bachmann, F., Hielscher, R., Schaeben, H., 2010. Texture analysis with MTEX-free and open source software toolbox. In: Solid State Phenomena, Vol. 160. Trans Tech Publ, pp. 63–68.

Basu, S., Dogan, E., Kondori, B., Karaman, I., Benzerga, A., 2017. Towards designing anisotropy for ductility enhancement: A theory-driven investigation in Mg-alloys. Acta Mater. 131, 349–362. http://dx.doi.org/10.1016/j.actamat.2017.02.046, URL http://www.sciencedirect.com/science/article/pii/S1359645417301374.

Becker, R., Lloyd, J., 2016. A reduced-order crystal model for HCP metals: application to Mg. Mech. Mater. 98, 98–110.

Benzerga, A.A., Besson, J., 2001. Plastic potentials for anisotropic porous solids. Eur. J. Mech. A Solids 20 (3), 397-434.

Benzerga, A.A., Thomas, N., Herrington, J.S., 2019. Plastic flow anisotropy drives shear fracture. Sci. Rep. 9 (1), 1425.

Beyerlein, I., Tomé, C., 2008. A dislocation-based constitutive law for pure Zr including temperature effects. Int. J. Plast. 24 (5), 867–895. http://dx.doi.org/10.1016/j.ijplas.2007.07.017, URL http://www.sciencedirect.com/science/article/pii/S074964190700109X.

Bohlen, J., Nrnberg, M.R., Senn, J.W., Letzig, D., Agnew, S.R., 2007. The texture and anisotropy of magnesium—zinc—rare earth alloy sheets. Acta Mater. 55 (6), 2101–2112. http://dx.doi.org/10.1016/j.actamat.2006.11.013, URL http://www.sciencedirect.com/science/article/pii/S1359645406008214. Bunge, H.-J., 2013. Texture Analysis in Materials Science: Mathematical Methods. Elsevier.

Cazacu, O., Barlat, F., 2004. A criterion for description of anisotropy and yield differential effects in pressure-insensitive metals. Int. J. Plast. 20 (11), 2027–2045. Cheng, J., Ghosh, S., 2015. A crystal plasticity FE model for deformation with twin nucleation in magnesium alloys. Int. J. Plast. 67, 148–170.

Cheng, J., Ghosh, S., 2017. Crystal plasticity finite element modeling of discrete twin evolution in polycrystalline magnesium. J. Mech. Phys. Solids 99, 512–538. Chun, Y., Davies, C., 2011. Negative lateral strain ratio induced by deformation twinning in magnesium alloy AZ31. Mater. Sci. Eng. A 528 (15), 4941–4946.

Foley, D., Al-Maharbi, M., Hartwig, K., Karaman, I., Kecskes, L., Mathaudhu, S., 2011. Grain refinement vs. crystallographic texture: Mechanical anisotropy in a magnesium alloy. Scr. Mater. 64 (2), 193–196.

Friedrich, H., Schumann, S., 2001. Research for a "new age of magnesium" in the automotive industry. J. Mater Process. Technol. 117 (3), 276–281. http://dx.doi.org/10.1016/S0924-0136(01)00780-4, URL http://www.sciencedirect.com/science/article/pii/S0924013601007804.

- Gehrmann, R., Frommert, M.M., Gottstein, G., 2005. Texture effects on plastic deformation of magnesium. Mater. Sci. Eng. A 395 (1), 338–349. http://dx.doi.org/10.1016/j.msea.2005.01.002, URL http://www.sciencedirect.com/science/article/pii/S0921509305000377.
- Graff, S., Brocks, W., Steglich, D., 2007. Yielding of magnesium: From single crystal to polycrystalline aggregates. Int. J. Plast. 23 (12), 1957–1978. http://dx.doi.org/10.1016/j.ijplas.2007.07.009. URL http://www.sciencedirect.com/science/article/pii/S0749641907001076.
- Guo, X., Chapuis, A., Wu, P., Agnew, S., 2015. On twinning and anisotropy in rolled Mg alloy AZ31 under uniaxial compression. Int. J. Solids Struct. 64–65, 42–50. http://dx.doi.org/10.1016/j.ijsolstr.2015.03.012, URL http://www.sciencedirect.com/science/article/pii/S0020768315001274.
- Habib, S.A., Khan, A.S., Gnupel-Herold, T., Lloyd, J.T., Schoenfeld, S.E., 2017. Anisotropy, tension-compression asymmetry and texture evolution of a rare-earth-containing magnesium alloy sheet, ZEK100, at different strain rates and temperatures: Experiments and modeling. Int. J. Plast. 95, 163–190. http://dx.doi.org/10.1016/j.ijplas.2017.04.006, URL http://www.sciencedirect.com/science/article/pii/S0749641916302224.
- Habib, S.A., Lloyd, J.T., Meredith, C.S., Khan, A.S., Schoenfeld, S.E., 2019. Fracture of an anisotropic rare-earth-containing magnesium alloy (ZEK100) at different stress states and strain rates: Experiments and modeling. Int. J. Plast. 122, 285–318. http://dx.doi.org/10.1016/j.ijplas.2019.07.011, URL http://www.sciencedirect.com/science/article/pii/S0749641919301147.
- Hill, R., 1948. A theory of the yielding and plastic flow of anisotropic metals. Proc. R. Soc. Lond. Ser. A Math. Phys. Eng. Sci. 193 (1033), 281-297.
- Hong, S.-G., Park, S.H., Lee, C.S., 2010. Role of {1012} twinning characteristics in the deformation behavior of a polycrystalline magnesium alloy. Acta Mater. 58 (18), 5873–5885.
- Hutchinson, W., Barnett, M., 2010. Effective values of critical resolved shear stress for slip in polycrystalline magnesium and other hcp metals. Scr. Mater. 63 (7), 737–740. http://dx.doi.org/10.1016/j.scriptamat.2010.05.047, URL http://www.sciencedirect.com/science/article/pii/S1359646210003726.
- Imandoust, A., Barrett, C., Al-Samman, T., Inal, K., El Kadiri, H., 2017. A review on the effect of rare-earth elements on texture evolution during processing of magnesium alloys. J. Mater. Sci. 52 (1), 1–29.
- Indurkar, P.P., Baweja, S., Perez, R., Vuppuluri, A., Joshi, S.P., 2020. Mapping anisotropy and triaxiality effects in magnesium alloys. In: Jordon, J.B., Miller, V., Joshi, V.V., Neelameggham, N.R. (Eds.), Magnesium Technology 2020. Springer International Publishing, Cham, pp. 321–328.
- Indurkar, P.P., Joshi, S.P., 2019. Void growth and coalescence in porous plastic solids with sigmoidal hardening. J. Appl. Mech. 86 (9), 091001. http://dx.doi.org/10.1115/1.4043519.
- Kale, C., Rajagopalan, M., Turnage, S., Hornbuckle, B., Darling, K., Mathaudhu, S., Solanki, K., 2018. On the roles of stress-triaxiality and strain-rate on the deformation behavior of AZ31 magnesium alloys. Mater. Res. Lett. 6 (2), 152–158.
- Kalidindi, S.R., 1998. Incorporation of deformation twinning in crystal plasticity models. J. Mech. Phys. Solids 46 (2), 267-290.
- Keralavarma, S., Benzerga, A., 2010. A constitutive model for plastically anisotropic solids with non-spherical voids. J. Mech. Phys. Solids 58 (6), 874-901.
- Keralavarma, S., Hoelscher, S., Benzerga, A., 2011. Void growth and coalescence in anisotropic plastic solids. Int. J. Solids Struct. 48 (11), 1696-1710.
- Khan, A.S., Pandey, A., Gnupel-Herold, T., Mishra, R.K., 2011. Mechanical response and texture evolution of AZ31 alloy at large strains for different strain rates and temperatures. Int. J. Plast. 27 (5), 688–706. http://dx.doi.org/10.1016/j.ijplas.2010.08.009, URL http://www.sciencedirect.com/science/article/pii/S0749641910001142.
- Knezevic, M., Levinson, A., Harris, R., Mishra, R.K., Doherty, R.D., Kalidindi, S.R., 2010. Deformation twinning in AZ31: influence on strain hardening and texture evolution. Acta Mater. 58 (19), 6230–6242.
- Kondori, B., 2015. Ductile Fracture of Magnesium Alloys: Characterization and Modeling (Ph.D. thesis).
- Kondori, B., Benzerga, A.A., 2014. Effect of stress triaxiality on the flow and fracture of Mg alloy AZ31. Metall. Mater. Trans. A 45 (8), 3292–3307. http://dx.doi.org/10.1007/s11661-014-2211-7.
- Kondori, B., Benzerga, A., 2015. On the notch ductility of a magnesium-rare earth alloy. Mater. Sci. Eng. A 647, 74–83. http://dx.doi.org/10.1016/j.msea.2015. 08.077, URL http://www.sciencedirect.com/science/article/pii/S0921509315303257.
- Kondori, B., Benzerga, A., 2017. Modeling damage accumulation to fracture in a magnesium-rare earth alloy. Acta Mater. 124, 225-236.
- Kondori, B., Madi, Y., Besson, J., Benzerga, A., 2018. Evolution of the 3D plastic anisotropy of HCP metals: Experiments and modeling. Int. J. Plast..
- Kumar, M.A., Beyerlein, I.J., Tomé, C.N., 2017. A measure of plastic anisotropy for hexagonal close packed metals: Application to alloying effects on the formability of Mg. J. Alloys Compd. 695, 1488–1497.
- Lee, B.H., Park, S.H., Hong, S.-G., Park, K.-T., Lee, C.S., 2011. Role of initial texture on the plastic anisotropy of Mg—3Al—1Zn alloy at various temperatures. Mater. Sci. Eng. A 528 (3), 1162–1172. http://dx.doi.org/10.1016/j.msea.2010.10.065, URL http://www.sciencedirect.com/science/article/pii/S0921509310012438.
- Lee, M.-G., Wagoner, R., Lee, J., Chung, K., Kim, H., 2008. Constitutive modeling for anisotropic/asymmetric hardening behavior of magnesium alloy sheets. Int. J. Plast. 24 (4), 545–582.
- Lloyd, J., Ligda, J., Williams, C., 2020. Pre-twinning alters shock-induced microstructure evolution in magnesium. Materialia 100606. http://dx.doi.org/10.1016/j.mtla.2020.100606, URL http://www.sciencedirect.com/science/article/pii/S2589152920300235.
- Lloyd, J.T., Priddy, M.W., 2017. Simulating strain localization in rolled magnesium. Acta Mater. 129, 149–158.
- Lou, X., Li, M., Boger, R., Agnew, S., Wagoner, R., 2007. Hardening evolution of AZ31B Mg sheet. Int. J. Plast. 23 (1), 44-86.
- Meredith, C.S., Lloyd, J.T., Sano, T., 2016. The quasi-static and dynamic response of fine-grained Mg alloy AMX602: An experimental and computational study. Mater. Sci. Eng. A 673, 73–82.
- Miller, V.M., Berman, T.D., Beyerlein, I.J., Jones, J.W., Pollock, T.M., 2016. Prediction of the plastic anisotropy of magnesium alloys with synthetic textures and implications for the effect of texture on formability. Mater. Sci. Eng. A 675, 345–360. http://dx.doi.org/10.1016/j.msea.2016.08.063, URL http://www.sciencedirect.com/science/article/pii/S0921509316309765.
- Mordike, B., Ebert, T., 2001. Magnesium: Properties applications potential. Mater. Sci. Eng. A 302 (1), 37–45. http://dx.doi.org/10.1016/S0921-5093(00)01351-4, URL http://www.sciencedirect.com/science/article/pii/S0921509300013514.
- Neil, C.J., Agnew, S.R., 2009. Crystal plasticity-based forming limit prediction for non-cubic metals: Application to Mg alloy AZ31B. Int. J. Plast. 25 (3), 379–398. http://dx.doi.org/10.1016/j.ijplas.2008.05.003, URL http://www.sciencedirect.com/science/article/pii/S0749641908000764.
- Nemcko, M.J., Li, J., Wilkinson, D.S., 2016a. Effects of void band orientation and crystallographic anisotropy on void growth and coalescence. J. Mech. Phys. Solids 95, 270–283.
- Nemcko, M.J., Qiao, H., Wu, P., Wilkinson, D.S., 2016b. Effects of void fraction on void growth and linkage in commercially pure magnesium. Acta Mater. 113, 68-80.
- Nitin, C., Ricardo A., L., Oana, C., Benoit, R.-B., Raja K., M., Frédéric, B., 2015. Combined effects of anisotropy and tension–compression asymmetry on the torsional response of AZ31 Mg. International Journal of Solids and Structures 58, 190–200. http://dx.doi.org/10.1016/j.ijsolstr.2015.01.001, http://www.sciencedirect.com/science/article/pii/S0020768315000037.
- Nixon, M.E., Cazacu, O., Lebensohn, R.A., 2010. Anisotropic response of high-purity α -titanium: Experimental characterization and constitutive modeling. Int. J. Plast. 26 (4), 516–532.
- de Oca Zapiain, D.M., Kalidindi, S.R., 2019. Localization models for the plastic response of polycrystalline materials using the material knowledge systems framework. Modelling Simulation Mater. Sci. Eng. 27 (7), 074008.
- Oppedal, A., Kadiri, H.E., Tomé, C., Vogel, S.C., Horstemeyer, M., 2013. Anisotropy in hexagonal close-packed structures: improvements to crystal plasticity approaches applied to magnesium alloy. Phil. Mag. 93 (35), 4311–4330. http://dx.doi.org/10.1080/14786435.2013.827802.
- Pineau, A., Benzerga, A.A., Pardoen, T., 2016. Failure of metals I: Brittle and ductile fracture. Acta Mater. 107, 424-483.

- Plunkett, B., Cazacu, O., Barlat, F., 2008. Orthotropic yield criteria for description of the anisotropy in tension and compression of sheet metals. Int. J. Plast. 24 (5), 847–866.
- Prasad, N.S., Narasimhan, R., Suwas, S., 2016. Numerical simulations of cylindrical void growth in Mg single crystals. Int. J. Fract. 200 (1-2), 159-183.
- Prasad, N.S., Narasimhan, R., Suwas, S., 2018. Effect of notch acuity on the fracture behavior of AZ31 Mg alloy. Eng. Fract. Mech. 187, 241-261.
- Qiao, H., Agnew, S., Wu, P., 2015. Modeling twinning and detwinning behavior of Mg alloy ZK60A during monotonic and cyclic loading. Int. J. Plast. 65, 61-84.
- Quey, R., Dawson, P., Barbe, F., 2011. Large-scale 3D random polycrystals for the finite element method: Generation, meshing and remeshing. Comput. Methods Appl. Mech. Engrg. 200 (17), 1729–1745. http://dx.doi.org/10.1016/j.cma.2011.01.002, URL http://www.sciencedirect.com/science/article/pii/S004578251100003X.
- Selvarajou, B., Joshi, S.P., Benzerga, A.A., 2017. Three dimensional simulations of texture and triaxiality effects on the plasticity of magnesium alloys. Acta Mater. 127. 54–72.
- Selvarajou, B., Joshi, S.P., Benzerga, A.A., 2019. Void growth and coalescence in hexagonal close packed crystals. J. Mech. Phys. Solids 125, 198-224.
- Selvarajou, B., Kondori, B., Benzerga, A.A., Joshi, S.P., 2016. On plastic flow in notched hexagonal close packed single crystals. J. Mech. Phys. Solids 94, 273–297. Selvarajou, B., Shin, J.-H., Ha, T.K., Choi, I.-s., Joshi, S.P., Han, H.N., 2014. Orientation-dependent indentation response of magnesium single crystals: modeling and experiments. Acta Mater. 81, 358–376.
- Song, B., Guo, N., Liu, T., Yang, Q., 2014. Improvement of formability and mechanical properties of magnesium alloys via pre-twinning: A review. Mater. Des. (1980–2015) 62, 352–360.
- Staroselsky, A., Anand, L., 2003. A constitutive model for HCP materials deforming by slip and twinning: application to magnesium alloy AZ31B. Int. J. Plast. 19 (10), 1843–1864.
- Steglich, D., Tian, X., Besson, J., 2016. Mechanism-based modelling of plastic deformation in magnesium alloys. Eur. J. Mech. A Solids 55, 289-303.
- Stewart, J.B., Cazacu, O., 2011. Analytical yield criterion for an anisotropic material containing spherical voids and exhibiting tension-compression asymmetry. Int. J. Solids Struct. 48 (2), 357–373.
- Tari, D.G., Worswick, M., Ali, U., Gharghouri, M., 2014. Mechanical response of AZ31B magnesium alloy: Experimental characterization and material modeling considering proportional loading at room temperature. Int. J. Plast. 55, 247–267. http://dx.doi.org/10.1016/j.ijplas.2013.10.006, URL http://www.sciencedirect.com/science/article/pii/S0749641913001976.
- Wang, Y., Choo, H., 2014. Influence of texture on Hall-Petch relationships in an Mg alloy. Acta Mater. 81, 83–97. http://dx.doi.org/10.1016/j.actamat.2014.08.023, URL http://www.sciencedirect.com/science/article/pii/S1359645414006247.
- Wang, H., Wu, P., Boyle, K., Neale, K., 2011. On crystal plasticity formability analysis for magnesium alloy sheets. Int. J. Solids Struct. 48 (6), 1000–1010. http://dx.doi.org/10.1016/ji.jisolstr.2010.12.004, URL http://www.sciencedirect.com/science/article/pii/S0020768310004403.
- Wang, H., Wu, P., Gharghouri, M., 2010. Effects of basal texture on mechanical behaviour of magnesium alloy AZ31B sheet. Mater. Sci. Eng. A 527 (15), 3588–3594. http://dx.doi.org/10.1016/j.msea.2010.02.050, URL http://www.sciencedirect.com/science/article/pii/S0921509310002157.
- Wang, H., Wu, P., Tomé, C., Wang, J., 2012. A constitutive model of twinning and detwinning for hexagonal close packed polycrystals. Mater. Sci. Eng. A 555, 93–98. http://dx.doi.org/10.1016/j.msea.2012.06.038, URL http://www.sciencedirect.com/science/article/pii/S0921509312008635.
- Wu, X., Proust, G., Knezevic, M., Kalidindi, S., 2007. Elastic-plastic property closures for hexagonal close-packed polycrystalline metals using first-order bounding theories. Acta Mater. 55 (8), 2729–2737.
- Thang, J., Joshi, S.P., 2012. Phenomenological crystal plasticity modeling and detailed micromechanical investigations of pure magnesium. J. Mech. Phys. Solids 60 (5), 945–972.
- Zhang, J., Wei, Q., Joshi, S.P., 2016. Effects of reinforcement morphology on the mechanical behavior of magnesium metal matrix composites based on crystal plasticity modeling. Mech. Mater. 95, 1–14.
- Zhang, E., Yin, D., Xu, L., Yang, L., Yang, K., 2009. Microstructure, mechanical and corrosion properties and biocompatibility of Mg—Zn—Mn alloys for biomedical application. Mater. Sci. Eng.: C 29 (3), 987–993. http://dx.doi.org/10.1016/j.msec.2008.08.024, URL http://www.sciencedirect.com/science/article/pii/S0928493108002117
- Zhou, G., Jain, M.K., Wu, P., Shao, Y., Li, D., Peng, Y., 2016. Experiment and crystal plasticity analysis on plastic deformation of AZ31B Mg alloy sheet under intermediate temperatures: How deformation mechanisms evolve. Int. J. Plast. 79, 19–47.